



UNIVERSITÀ DEGLI STUDI DI PADOVA

DIPARTIMENTO DI FISICA E ASTRONOMIA
“GALILEO GALILEI”

CORSO DI LAUREA MAGISTRALE IN ASTRONOMIA

**A SIX-DIMENSIONAL PHASE SPACE STUDY
OF NGC 6752**

RELATORE

GIOVANNI CARRARO
UNIVERSITÀ DI PADOVA

CO-RELATORI

SIMONE ZAGGIA, YAZAN AL MOMANY
INAF-OAPD

LAUREANDO

HITESH N. LALA

CONTRORELATORE

ANTONINO MILONE
UNIVERSITÀ DI PADOVA

ANNO ACCADEMICO 2018/19

“UNDERSTANDING IS ECSTASY.”

CARL SAGAN

Abstract

GLOBULAR CLUSTERS are one of the oldest entities in the universe and they have been studied meticulously for over half a century. However, many important questions remain unanswered about them. One of them is how the dynamics of a globular cluster affects its stellar populations. We try to address this by studying the globular cluster NGC 6752. This cluster was chosen as the focus of the thesis as it harbors an exotic population of stars and exhibits peculiar photometric and dynamic properties. The cluster holds a vital key in fully understanding the inter-dependence of stellar and dynamic evolution in a globular cluster.

We present multi-band, wide-field photometry of NGC 6752 observed with ESO VLT Survey Telescope (VST) combined with similar epoch Gaia DR2 astrometry and other large scale surveys (HUGS, 2MASS, VHS, GALEX, WISE). The reduction of the data was carried out using ESO's reduction pipeline Alambic refined for VST OmegaCam. Preliminary aperture photometry was performed using SExtractor and PSF photometry was carried out using DAOPHOT. Reduction and photometric extraction were implemented in an automated pipeline over all filters, all exposure times, and all the individual CCDs of OmegaCAM.

The independently photometrised plethora of catalogs were woven together meticulously to produce a single master catalog of all filters. This was matched with a multitude of external surveys to get a comprehensive astro-photometric catalog of NGC 6752. The stars in this catalog were cleaned along newly computed fiducial sequences and Gaia proper motions.

The member stars remaining after the culling processes were used to derive the number density profile of the cluster. These count were complemented with Hubble Space Telescope data available for the cluster's internal regions (from the HUGS project). King, Wilson and LIMEPY models were fit to the density profile to gauge the dynamical properties of the cluster.

Owing to the 1 square degree field of view of our data, star counts were performed for the evolved stars along the entire radial range of the cluster. These were used to calculate pertinent population parameters R and R_2 and to derive the radial distribution of these stars. The radial distribution unveiled a puzzling observable about the cluster: a sudden disappearance of horizontal branch stars within 6 and 13 arcminutes from the centre in the r magnitude range $16 \lesssim r \lesssim 17$, which can be ascribed to an as yet unidentified mechanism pertaining to the dynamics and stellar evolution of the cluster.

Contents

ABSTRACT	v
LIST OF FIGURES	ix
LIST OF TABLES	xi
1 INTRODUCTION	1
1.1 Multiple Stellar Populations	2
1.2 Dynamics	3
1.3 Morphology	5
1.4 NGC 6752	7
1.4.1 Exotic Population	8
1.4.2 The BSS bimodality	9
1.4.3 The HB Conundrum	11
1.4.4 The AGB Perplexion	12
2 DATA AND REDUCTION	15
2.1 Instrument	15
2.2 Data-set	16
2.3 Reduction	19
2.3.1 Alambic	19
3 PHOTOMETRY	27
3.1 Source Extractor	28
3.2 DAOPHOT II	29
3.3 DAOMATCH & DAOMASTER	31
3.4 Aperture Correction	33
3.5 Calibration	34
4 THE CATALOG	37
4.1 Stitching	37
4.2 Combining Deep-Shallow	38
4.3 Combining Filters	39
4.4 Matching external surveys	42
4.4.1 Procuring the catalogs	42

4.4.2	Gaia	42
4.4.3	GALEX	43
4.4.4	2MASS + VHS	43
4.4.5	WISE	45
4.4.6	Stetson's Homogeneous Photometry	45
4.4.7	HUGS	45
4.5	Culmination	45
5	ANALYSIS AND RESULTS	49
5.1	Membership	49
5.1.1	CMD cleaning	49
5.1.2	Proper Motion cleaning	52
5.2	Number Density Profile	54
5.2.1	HST number density profile	56
5.2.2	Fitting Dynamic Models	58
5.3	Isochrone fitting	60
5.4	H α CMD	61
5.5	Star counts of evolved stars	62
5.5.1	R parameter	62
5.5.2	R_2 parameter	63
5.5.3	Radial Distribution	67
6	CONCLUSIONS	71
	ACKNOWLEDGMENTS	73
	REFERENCES	75

Listing of figures

1.1	Multiple Stellar Populations detected in GCs	2
1.2	Cycle of core-collapse	5
1.3	NGC 6752 observed using WFI and HST	8
1.4	NGC 6752 observed in UV and X-ray wavelengths	10
1.5	Multiple Stellar Populations detected in NGC 6752	10
1.6	Various sub-populations of a GC	11
2.1	OmegaCAM CCD mosaic	16
2.2	Throughput curves of OmegaCAM filters	17
2.3	OmegaCAM central vignetted cross	17
2.4	Alambic data reduction flowchart	20
2.5	Calibration frames	21
2.6	Raw image and weight map	22
2.7	Standard field	22
2.8	Fringing map for i-filter	23
2.9	Illumination map for the u-filter	24
2.10	A u-filter reduced science frame	25
2.11	An i-filter reduced science frame	25
3.1	Preliminary flowchart of SExtractor	28
3.2	Articulate flowchart of SExtractor	30
3.3	Instrumental color-magnitude diagram	32
3.4	Aperture correction for a single chip	34
3.5	Calibrating using SkyMapper zero-points	35
4.1	Stitching single chips of the CCD	38
4.2	Refining separation distance in matches	40
4.3	Calibrated u, g, r color magnitude diagrams	41
4.4	Calibrated r, i, z color magnitude diagrams	42
4.5	Gaia color magnitude diagrams	44
4.6	Color magnitude diagrams in infrared wavelengths	44
4.7	Extinction map for NGC 6752	46
5.1	i vs r-i CMD	50
5.2	Main sequence fiducial line	51
5.3	RBG and HB fiducial sequence	51

5.4	Selection based on CMD	53
5.5	Proper motion cleaning along RA, DEC	53
5.6	Selection on total proper motion	55
5.7	Selection of cluster members	55
5.8	Selecting HUGS data	56
5.9	Calculating the centre	57
5.10	Combined number density profile	58
5.11	Fitting of dynamic models	59
5.12	Best fitting PARSEC isochrone	61
5.13	Signs of H α excess	62
5.14	Star counts along OmegaCAM CMDs	64
5.15	Counting stars in the HST CMD	64
5.16	R_2 parameter	65
5.17	Radial distribution of evolved stars	66
5.18	Missing population in the HB	66
5.19	Dividing the HB	67
5.20	Star counts using various bin sizes	68
5.21	Smoothed star counts of the HB branches	69

Listing of tables

1.1	Parameters of NGC 6752	9
2.1	Details of the data-set	18
4.1	Number of stars matched across filters	41
4.2	Details of external matched surveys	43
4.3	Magnitudes in the final catalog	46
5.1	Selecting member stars	54
5.2	Best fitting dynamic models	60

Astronomy compels the soul to look upward, and leads us from this world to another.

Plato

1

Introduction

GLOBULAR CLUSTERS have been under the proverbial microscope of astronomers for over half a century. The name globular is derived from the Latin word *globulus* which translates to a small sphere. However, these clusters appear small due to their distance from us but are orders of magnitude larger in size than Earth. They are huge, densely packed, spherical agglomerations of stars. A globular cluster can contain anywhere from 10^4 to 10^6 inhabitants within itself and be as wide as 100 pc in diameter.

Conventionally (Herschel, 1789), globular clusters were considered to be spherically symmetric, isotropic, non-rotating systems, chemically homogeneous and as textbook examples of simple stellar populations (SSPs). With the advent of technology - CCD photometry and high-resolution, multi-object spectroscopy in particular - data of unparalleled quality and quantity have been produced. This, in turn, has led to many revelations in our understanding of globular clusters (GCs). GCs are now considered as spherically asymmetric, anisotropic, rotating stellar aggregations, with chemical peculiarities a significant departure from the erstwhile elementary assumptions.

Each massive galaxy contains a system of globular clusters that orbits its core. Milky Way consists of approximately 150 globular clusters (Harris, 1996) whereas the elliptical galaxy M87 harbours more than 13,000 of them (McLaughlin et al., 1994). As a result, GCs are thought to be the philosopher's stone against which theories of galaxy formation and evolution can be put to test. For a review, see Kruijssen (2014).

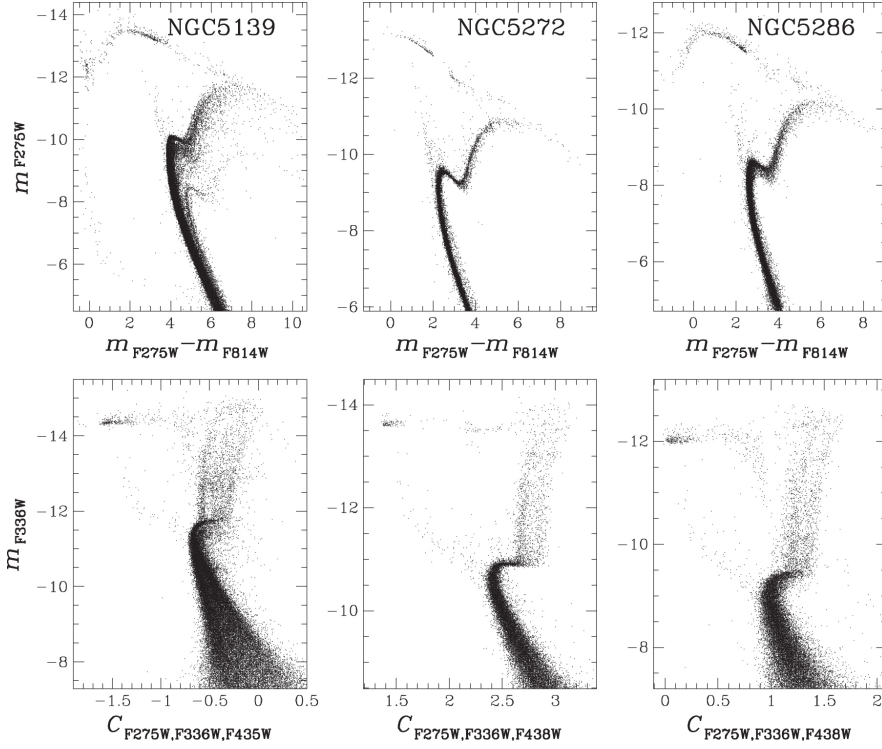


Figure 1.1: An example of multiple stellar populations detected in three different globular clusters using Hubble Space Telescope photometry (Piotto et al., 2015).

1.1 MULTIPLE STELLAR POPULATIONS

Historically, GCs have been considered as SSPs (Renzini & Buzzoni, 1986). Stars within a simple stellar population are considered to be contemporary i.e. all the stars formed in a single burst of star formation. They are assumed to have the same initial composition and different mass, distributed according to an initial mass function. In a Hertzsprung-Russell Diagram (HRD), stars of an SSP are located along an isochrone (meaning “same age” in Greek). An SSP can be holistically described by the following parameters:

1. Age
2. Initial Mass Function (IMF)
3. Chemical Composition:
 - (a) Helium Mass Fraction (Y)
 - (b) Metallicity (Z)

The stars in an SSP are expected to have similar values of these parameters. If a collection of stars violates any one of these conditions, it can no longer be considered a *simple* stellar population. Since the study of Kraft (1979), there have been signs that GCs might not be SSPs as light-element abundance variations were detected in their stars. The cause of these anomalies was not easily discernible. It was thought the anomalies manifested due to varying internal mixing or differences in primordial composition or both. Recent high-resolution studies and multi-band photometry have shifted the paradigm and globular clusters are now considered harboring *Multiple* Stellar Populations (MSP, Gratton et al. 2004, Gratton et al. 2012, Bastian & Lardo 2018).

The multiple sequences in the Color Magnitude Diagram (CMD) of a GC are populated by stars having different chemical abundances. The elements associated with Hydrogen burning are the ones that display abundance variations. Many GCs exhibit evidence of Helium-enrichment in their second generation stars and also display complex anti-correlations in their light-element abundances (e.g. Sodium vs Oxygen and Nitrogen vs Carbon). This indicates that newer material has been processed via high-temperature proton capture nucleosynthesis. However, these multiple sequences cannot be detected easily in all CMDs. A combination of ultraviolet and blue filters is particularly adept at disentangling these populations (Milone et al., 2013). An example of MSPs in globular clusters is shown in Figure 1.1. Such MSPs have now been found in almost all GCs. In order to fully understand the intrinsic properties of globular clusters, it is imperative to amalgamate theoretical modelling with deep photometric and spectroscopic surveys that are aimed at detecting these multiple populations.

1.2 DYNAMICS

Globular clusters are not just probes of the dynamics of the galaxy but also peculiar dynamical bodies themselves. They can be regarded as the test particles of the galactic gravitational field. Moreover, as GCs have a mass in the range of $10^5 M_{\odot}$, dynamical processes fundamental to the understanding of stellar dynamics take place in these systems. To illustrate further:

1. Relaxation

Globular clusters are considered relaxed systems. After they are formed, the stars in the globular cluster begin to interact gravitationally with each other. As a result, the velocity of the interacting stars are steadily modified and the stars lose any history of their initially velocity (i.e. they are thermalized). The characteristic timescale at which this occurs for a GC is called the relaxation time. The relaxation time is expressed as a

function of the crossing time (or the dynamical time, τ_{cross}), which is the time taken by a star to cross the GC. According to [Binney & Tremaine \(2008\)](#), for a GC with N stars:

$$\tau_{rlx} = \frac{N}{8 \log(N)} \tau_{cross} \quad (1.1)$$

The mean relaxation time (τ_{rlx}) for globular clusters is 10^8 years ([Benacquista & Downing, 2013](#)), which is smaller than their age of 10^{10} years. Hence, GCs are regarded as relaxed systems. Cumulative effects of this dynamical relaxation pave the way for mass segregation.

2. Mass Segregation and Evaporation

Dynamical mass segregation is the process by which more massive stars move toward the center, while lighter ones tend to move farther away from the center. During a close encounter of two stars, they exchange both energy and momentum. Due to equipartition of energy, the velocities of the stars transform in such a way that their global velocity distribution approaches a Maxwellian. Since kinetic energy is proportional to mass times speed squared, equipartition requires the less massive members of a cluster to move faster. Thus, heavier stars will sink into lower orbits (i.e. orbits closer to the center of the cluster) leading to a mass segregation.

After relaxation, the speed of some low mass stars (residing at the far right tail of the Maxwellian) can be greater than the cluster's escape velocity, which leads to these stars leaving the cluster. This process that results in a stellar exodus is called evaporation. Even though GCs are tightly bound, many of them exhibit potential escaping stars ([de Boer et al., 2019](#)). Interaction of the cluster with the galactic tidal field can also lead to stripping of stars which aggravates evaporation.

3. Core Collapse

Due to the Virial theorem, the heat capacity of any finite gravitationally bound system (such as a globular cluster) is always negative. As a result, at any given moment the random motions of stars in a cluster's core can be considered to balance the gravitational potential of the stars' mutual attractions. When a fast-moving star escapes the gravitational pull of the cluster core, taking with it some kinetic energy, the core must shrink a little. The remaining stars have to move a bit faster to compensate for the increase in the gravitational binding energy of a denser core. More of them can then escape, and so the process repeats itself and accelerates.

This runaway gravo-thermal instability eventually leads to a rapid shrinking of the core of the cluster called as core collapse (see Figure 1.2). However, the interaction of stars in the collapsed core region causes tight binary systems (hard binaries) to form. As other stars interact with these hard binaries, they increase the energy in the core, which

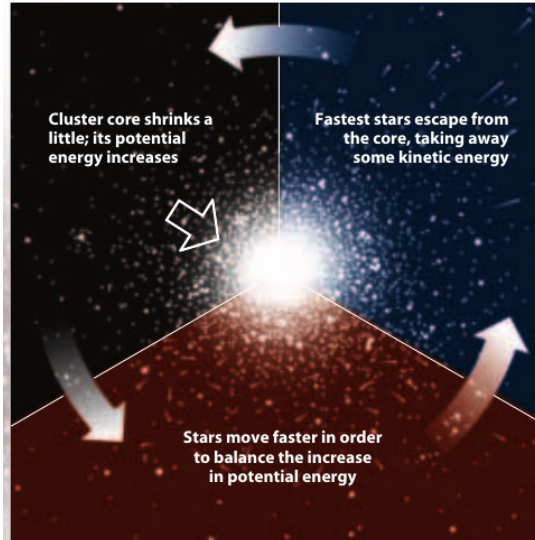


Figure 1.2: Pictorial representation of how a globular cluster undergoes core collapse in an attempt to maintain virial equilibrium. For details, see Section 1.2. Source: [Djorgovski \(1998\)](#).

limits the core collapse and leads to re-expansion of the cluster. The hard binaries act as dynamical energy reservoirs. About 20 % of the GCs observed have undergone core collapse as seen by their increasing luminosity toward the centre of the cluster ([Djorgovski & King, 1986](#)).

1.3 MORPHOLOGY

Globular clusters are approximately equivalent to isothermal spheres i.e. the velocity distribution of stars is almost independent of the position of the stars in the cluster (resembling a Maxwellian distribution). However, a singular isothermal sphere has infinite density at its centre and hence, infinite mass. To represent an isothermal sphere in a well-behaved manner at the origin, it is possible to define dimensionless variables, where the dimensionless radius variable (R) is given by:

$$R \equiv \frac{r}{r_0} \tag{1.2}$$

$$r_0 \equiv \sqrt{\frac{9\sigma^2}{4\pi G\rho_0}} \tag{1.3}$$

In equation 1.2, r is the distance from the centre and r_0 is the King radius (King, 1962) defined in equation 1.3, where ρ_0 is the central density, σ is the velocity dispersion scaling parameter and G is the gravitational constant. At the radius r_0 , the density within the system has fallen to 0.5013 of its central density ρ_0 . For a system with gravitational potential Φ , where a single particle has velocity v and total energy E , the relative potential Ψ and relative energy ε of the particle can be defined as

$$\Psi \equiv -\Phi + \Phi_0 \quad (1.4)$$

$$\varepsilon \equiv -E + \Phi_0 = \Phi_0 - \frac{1}{2}v^2 \quad (1.5)$$

where Φ_0 is some constant.

A modified form of an isothermal sphere is the King model, which resembles the isothermal sphere at small radii, where most of the stars have large values of ε , but gradually becomes less dense than the isothermal sphere at larger radii where ε tends to be lower. By suitably defining the constant gravitational potential Φ_0 so that at some critical relative energy $\varepsilon_0 = 0$, the phase-space distribution function of the King model can be defined so that:

- For $\varepsilon \gg 0$, King model and isothermal sphere are identical;
- For $\varepsilon \leq 0$, King model distribution function is zero

This leads to a family of self-similar models for the density distribution within the system that are defined by the central relative potential, $\Psi(0)$, where the radius is in units of the King radius (r_0). At the radius where Ψ falls to zero, the density (ρ) also falls to zero. This is the tidal radius (r_t , described below). The logarithm of the ratio of the tidal radius to the King radius defines the concentration of the cluster (c):

$$c \equiv \log_{10} \left(\frac{r_t}{r_0} \right) \quad (1.6)$$

Barring the King radius, the 3 important radii for a globular cluster are:

1. Core radius

The overall luminosity of the cluster steadily decreases with distance from the core,

and the core radius (r_c) is the distance at which the apparent surface luminosity has dropped by half of its peak value at the centre. Therefore, it is often used interchangeably with the King radius (r_0) The median value of r_c for GCs in Milky Way is around 1 pc (Binney & Tremaine, 2008).

2. Half-light radius

The distance from the core within which half of the total luminosity from the cluster is received is called as the half-light radius (r_h). This is typically larger than the core radius but smaller than 10 pc (van den Bergh, 2008).

3. Tidal radius

The distance from the center of the globular cluster at which the galactic gravitational field has more influence over the stars in the cluster than the cluster itself is called as the tidal radius (r_t or truncation radius). This is the distance at which the individual stars belonging to a cluster can be stripped away by the galaxy. Typical values for r_t are around 35-40 pc (de Boer et al., 2019).

Globular clusters harbour a multitude of RR Lyrae stars (Di Criscienzo et al., 2004) and other standard candles which constitute an important part of the cosmic distance ladder. Globular clusters as a group present a luminosity function which is also used as a standard candle under the assumption that GCs in other galaxies follow the same principles as those in Milky Way (Rejkuba, 2012). Absolute ages derived for GCs give a robust lower limit to the age of the universe. Apart from these pertinent astrophysical properties, GCs are host to very peculiar objects. To list a few: Blue straggler stars, Cataclysmic variables, X-ray binaries, Neutron stars, millisecond Pulsars, etc.

1.4 NGC 6752

NGC 6752 is one of the closest and brightest southern hemisphere globular clusters. It is at a distance of ~ 4.2 kpc from us and has an apparent magnitude of ~ 5.5 mag. It was first observed in 1826 by James Dunlop and was catalogued as GC 4484 by John Herschel in his 1864 study (Herschel, 1864). The cluster has been a focus of multitude of studies over the past half century with it being referenced in almost 2000 research papers. It has been the main focus of more than 200 extensive studies. The cluster's important properties are summarized in Table 1.1. Photometric studies have revealed that the luminosity function of the cluster exhibits clear signs of mass segregation (Ferraro et al., 1997) whereas dynamical studies have also revealed that it has undergone an era of core collapse (Djorgovski 1993,



(a) An image of NGC 6752 taken using the Wide Field Imager on the MPG/ESO 2.2-metre telescope at the La Silla Observatory in Chile.

(b) A 3.5×3.5 arcmin² image of NGC 6752 taken using the Hubble Space Telescope (HST)

Figure 1.3: High-resolution images of NGC 6752. Orientation in both the figures is: North is up and East is to the left.

Rubenstein & Bailyn 1997). No rotation in the cluster has yet been detected (Cordoni et al., 2019).

1.4.1 EXOTIC POPULATION

Existence of multiple stellar populations in NGC 6752 has been confirmed by space-based (Milone et al., 2013) as well as ground-based (Nardiello et al., 2015) photometry. Milone et al. (2013) showed that the CMD of NGC 6752 can be split into 3 components with varying light-element abundances. The CMD gets split into these components when a special combination of filters (described in the papers) is used. Along with them, Strömgren photometry is adept at disentangling multiple populations along the Red Giant Branch (RGB, Grundahl et al. 2002). These multiple populations have also been confirmed in the lower main sequence of NGC 6752 by employing deep Near-Infrared (NIR) photometry (Milone et al., 2019). Three different populations of M-dwarfs are detected in the NIR CMD of NGC 6752.

The cluster has been investigated extensively over a wide range of wavelength yet it doesn't cease to surprise. It is extremely bright in the ultraviolet wavelengths as seen in in Figure 1.4a. The stars lying along the horizontal branch (HB) of the cluster (discussed below) are the

Table 1.1: Basic parameters of NGC 6752. α_{J2000} , δ_{J2000} and l , b are geocentric and galactocentric positional coordinates, respectively. R_{\odot} is the heliocentric distance of the cluster and R_{GC} is the galactocentric distance. E(B-V) is color excess. r_c , r_h , r_t are the core, half-light, and tidal radii of the cluster, respectively, as explained in Section 1.3. R_v is the radial velocity and $\mu_{\alpha \cos(\delta)}$, μ_{δ} are proper motions in RA and DEC. Proper motion in R.A. is multiplied by $\cos(\delta)$ to compensate for the spherical geometry. All values taken from [Baumgardt et al. \(2019\)](#) and E(B-V) taken from [Gratton et al. \(2005\)](#).

Parameter	Value	Property	Value
α_{J2000}	$19^h 10^m 52.11^s$	Mass	$2.29 \pm 0.0310^5 M_{\odot}$
δ_{J2000}	$-59^{\circ}59'4''.4$	r_c	0.15 pc
l	336.493	r_h	2.38 pc
b	-25.628	r_t	61.97 pc
R_{\odot}	4.25 ± 0.09 kpc	R_v	-26.28 ± 0.16 km/s
R_{GC}	5.53 kpc	$\mu_{\alpha \cos(\delta)}$	-3.17 ± 0.01 (mas/yr)
E(B-V)	0.046 ± 0.005	μ_{δ}	-4.01 ± 0.01 (mas/yr)

major contributors to this UV light. The cluster plays host to a few low-mass X-ray binaries (see Figure 1.4b) and as many as 19 X-ray sources have already been detected by [Pooley et al. \(2002\)](#). Many of these sources have been confirmed in optical studies to be Cataclysmic Variables (such as Dwarf Novae, [Thomson et al. 2012](#)). NGC 6752 has also shown signs of gamma ray emissions from within its tidal radius ([Tam et al., 2011](#)) insinuating that it is home to multiple millisecond pulsars. Along with these special objects, the cluster also inhabits a myriad of variable stars that have been comprehensively catalogued by [Kaluzny & Thompson \(2009\)](#).

1.4.2 THE BSS BIMODALITY

A blue straggler star (BSS) is a main-sequence star more luminous and bluer than stars at the main sequence turnoff point for a cluster (see Figure 1.6). Since their discovery by [Sandage \(1953\)](#), numerous explanations regarding their formation have been put forth. However, the two most widely supported scenarios are:

1. They are current or former binary stars which are merging to create a single more massive star, potentially with a mass larger than that of stars at the main-sequence turn-off point. Since the density in GCs' core is very high, the chances of collisions between stars leading to a merger are higher, too.
2. They are a product of mass transfer between binary stars. As the more massive of the stars evolve and overflows its Roche lobe, mass will transfer to its companion resulting in a star more massive than those at the turn-off point.



(a) NGC 6752 as seen in a 786-second exposure at a wavelength of 1620 Angstroms with the Ultraviolet Imaging Telescope (UIT). The overexposed bright star about 4 arcminutes southwest of the cluster center is the foreground star HD 177999.



(b) A 2.5×2.5 arcmin² image of NGC 6752 taken using the Chandra X-ray Observatory. The image is a composite of observations from 0.5-6 keV taken from [Pooley et al. \(2002\)](#).

Figure 1.4: NGC 6752 observed in UV and X-ray wavelengths.

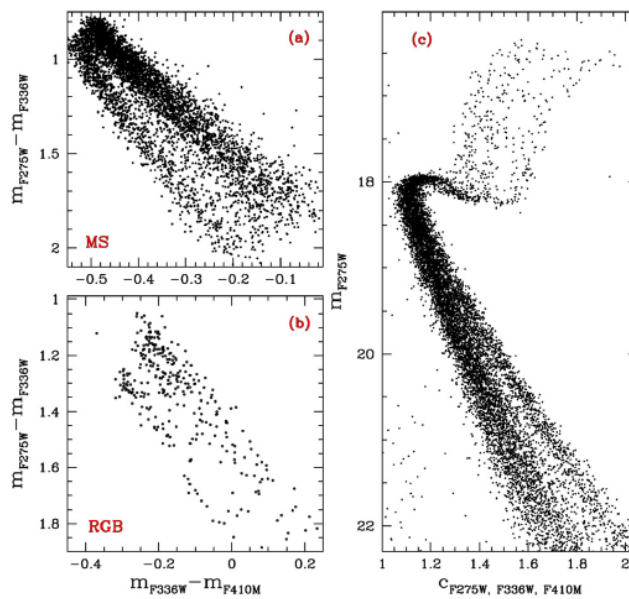


Figure 1.5: An example of multiple stellar populations detected in NGC 6752. The 3 different sequences along the Red Giant Branch and the Main-sequence in Panel (c) are easily discernible when a color-index magnitude diagram is produced using a particular combination of Hubble Space Telescope filters ([Milone et al., 2013](#)).

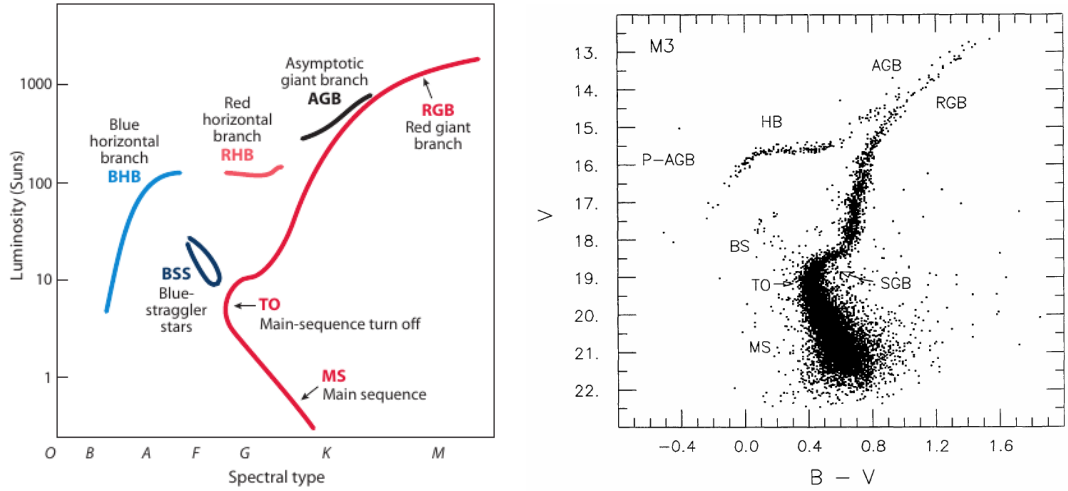


Figure 1.6: (Left) An artist's representation of a Hertzsprung-Russell diagram delineating the regions of various sub-populations of a globular cluster. (Right) Color Magnitude diagram of the globular cluster M3 (Renzini & Fusi Pecci, 1988) showing the same populations.

Both these mechanisms might be at play in NGC 6752 as a bimodal distribution of blue straggler stars has been detected in the cluster (Sabbi et al. 2004, Mapelli et al. 2006). It is hypothesized that collisional blue stragglers occupy the cluster's core and mass-transfer blue stragglers reside in the outskirts.

1.4.3 THE HB CONUNDRUM

Low-to-intermediate mass stars after going through a helium flash at the tip of the RGB start burning He in their cores along the Horizontal Branch (HB). On the HB, these stars have very similar core masses and thereby very similar luminosities. As a result, they constitute themselves along a *horizontal* sequence in the HRD (or the CMD). However, the size (and therefore temperature) of an HB star depends on the mass of the hydrogen envelope surrounding the He core. Smaller H envelopes lead to hotter stars. As a result, stars on the HB can cover an extended range of effective temperatures.

A prominent feature in a GC's HB is the RR Lyrae gap which encompasses the instability strip. The variable nature of stars lying in this region engenders the gap in the HB. Different GCs show different morphologies of their HB. The relative proportions of HB stars existing on the hotter end of the RR Lyr gap, within the gap, and to the cooler end of the gap varies sharply from cluster to cluster. It has been noted that metal-poor clusters show a bluer HB (more stars toward the hotter, left side of the gap), whereas metal-rich clusters present

a redder HB. However, some clusters with the same metallicity show starkly different HBs and some clusters with similar HB morphologies do have different metallicities (Sandage & Wallerstein, 1960). Therefore, a *second parameter* has long been sought to break this degeneracy and fully explain the HB morphology. Among the various candidates for the elusive second parameter, age, GC's mass, GC's central density, and He abundance are considered as the best candidates (Freeman & Norris 1981, Gratton et al. 2010).

The horizontal branch of NGC 6752 has been studied painstakingly over the past decade and with good reason. Like many other GCs, it showcases the following discontinuities: (i) the Grundahl jump at $\sim 11,500$ K (Grundahl et al., 1999) which marks the onset of the blue HB and (ii) the Momany jump (Momany et al. 2002, Momany et al. 2004) at $\sim 22,000$ K which delineates the beginning of the Extreme Horizontal Branch (EHB). The physical mechanism underneath the formation of the EHB still evades us. NGC 6752 will be paramount to finding a viable scenario for EHB formation as well as solving the second parameter problem.

1.4.4 THE AGB PERPLEXION

At the end of the HB lifetime, the core He burning comes to a halt and shifts to a shell surrounding the inert C-O core. This flags the beginning of the Asymptotic Giant Branch (AGB) phase. The AGB phase is the last evolutionary stage of intermediate and low-mass stars before they end their lives as white dwarfs. The time spent by stars in the AGB is only a few percent of the time spent in the HB.

In spite of harboring such an exotica of stars, NGC 6752 showed a dearth of 2nd generation AGB stars in its CMDs (Campbell et al., 2013). It was assumed that this might probably have its origin in the fact that He-enhanced 2nd generation stars have a shorter lifetime (Charbonnel et al., 2013). However, recent studies have confirmed that the AGB of NGC 6752 is well-populated and it displays the expected correlations/anti-correlations among the light-element abundances (Mucciarelli et al., 2019).

All in all, the cluster possesses an interesting stellar population and has inhabitants representing each section of the CMD. The aforementioned features and many others like them, make NGC 6752 an important cog in fully understanding stellar evolution and how it is affected by the dynamics of a globular cluster.

The thesis is divided into 6 chapters.

The 2nd Chapter describes the data-set used in the thesis and the strategies used to reduce it. The 3rd Chapter sheds light on how Aperture and PSF photometry were carried out for our complex data-set and elaborates the pipeline built to automatize the entire procedure. Obtaining an extensive catalog which comprises a multitude of photometric and astrometric properties of NGC 6752 is discussed in Chapter 4. Chapter 5 delves deeper into how the members of the cluster were selected and how other photometric analyses were undertaken. Chapter 6 summaries the results and outlines the foundation laid down by this thesis for future works.

At the end of each chapter, the status of our data at the beginning of that chapter and the status at the end of it has been elucidated in a few lines. They are the takeaways of each chapter; they facilitate the reader in assessing the progress made over the course of a single chapter.

As we look out into the Universe and identify the many accidents of physics and astronomy that have worked together to our benefit, it almost seems as if the Universe must in some sense have known that we were coming.

Freeman Dyson

2

Data and Reduction

This chapter elaborates the data-set and how it was procured. It also discusses the various strategies implemented in reducing the data.

2.1 INSTRUMENT

NGC 6752 was observed using the wide-field imager OmegaCAM situated at ESO's VLT Survey Telescope (VST, [Arnaboldi et al. 1998](#), [Kuijken et al. 2002](#), [Kuijken 2011](#)). VST is a 2.65 m modified Ritchie-Cr tien telescope located at the Paranal platform of ESO's Very Large Telescope in Chile. It is specifically designed for wide-field imaging and OmegaCAM is the sole instrument on the telescope mounted at its Cassegrain focus.

OmegaCAM is a 256-megapixel optical camera with physical dimensions of $26 \times 26 \text{ cm}^2$. It has a $1 \times 1 \text{ degree}^2$ field of view at a resolution of $0''.216/\text{pixel}$. The camera is a 32-CCD detector mosaic with each CCD roughly 2000 pixels in width and 4000 pixels in height. The CCDs are thinned, blue-sensitive, 3-edge butttable CCD 44-82 devices from e2v of high cosmetic quality. Each chip subtends approximately $7'.3 \times 14'.6$ on the sky. There are narrow gaps between the individual CCDs (see Figure 2.1), resulting in 1.5 mm wide, insensitive strips across the focal plane. In addition, there are two broader insensitive bands, each 5.7 mm wide, which is where the CCD bond wires are. The gaps translate to $25''$ and $85''$ on the sky respectively. Reflection of starlight off the wires is prevented with black metal strips

mounted above them.

OmegaCAM data are taken in the context of a calibration plan that ensures that all data can be photometrically and astrometrically calibrated to 0.05 magnitudes and 0.1 arcseconds r.m.s. precision, respectively. In addition to the science CCDs, the focal plane also contains four auxiliary CCDs. Two of these are used for auto-guiding, so that both field position and rotation can be tracked accurately. The other two auxiliary CCDs are mounted 2 mm outside the focal plane and are used for recording defocused star images for curvature wavefront sensing and controlling the active optics system of the VST.

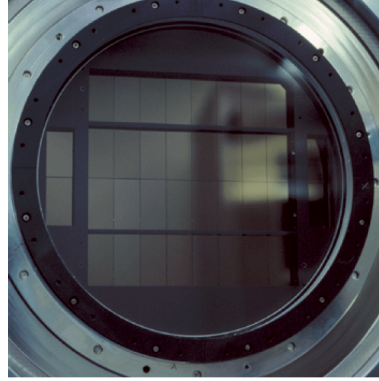


Figure 2.1: The CCD array of OmegaCAM in its dewar. Source: [Kuijken \(2011\)](#).

A filter exchange mechanism permits observations through any one of 12 filters viz. Sloan ugriz set, Johnson B and V filters, several narrow-band filter mosaics, a Strömgren v filter, and a special calibration u-g-r-i filter. A large shutter is used to define precisely the length of the exposures and is able to carry out observations for as short as a 0.1 seconds. Coupled with these features, the sky coverage, angular resolution, and low seeing were the reasons VST was chosen to study NGC 6752. It enabled us to study the cluster’s crowded centre along with its outskirts at greater depths.

2.2 DATA-SET

The data-set comprised of images taken over a period of 2 years in the broadband SDSS u, g, r, i, z filters. Along with these wide filters, we had observations taken in the narrow-band H α filter. This filter has been designed specifically for the VPHAS+ survey ([Drew et al., 2014](#)). The throughput curves for these filters are shown in Fig. 2.2 and the central wavelengths along with their effective widths are shown in Table 2.1.

The observations were carried out during ESO Period 103 and 104 and were taken in *jitter* mode to account for the vertical gaps in the CCD array. The observation strategy was set in a manner such that the cluster’s central region was always observed from the same CCD - CCD # 84 (Chip 12) - even after accounting for the jitter.

The Sloan u,g,r,i,z filters are monolithic and as a result, a small jitter pattern is enough to cover the areas missed due to vertical gaps of 25". The H α filter is segmented, thereby pre-

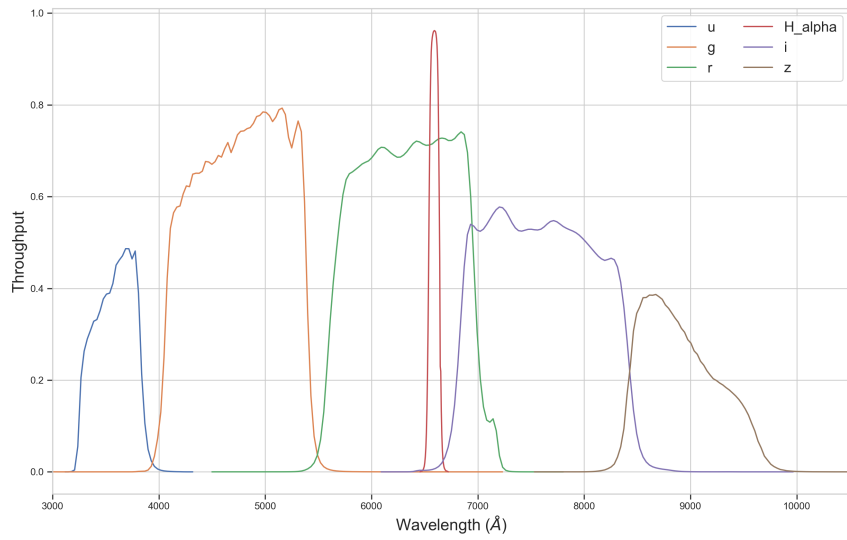


Figure 2.2: Throughput curves of the Sloan ugriz and H α filters. The central wavelengths and effective widths of the filters are given in Table 2.1. The curves were obtained from Spanish Virtual Observatory's [Filter Profile Service](#).

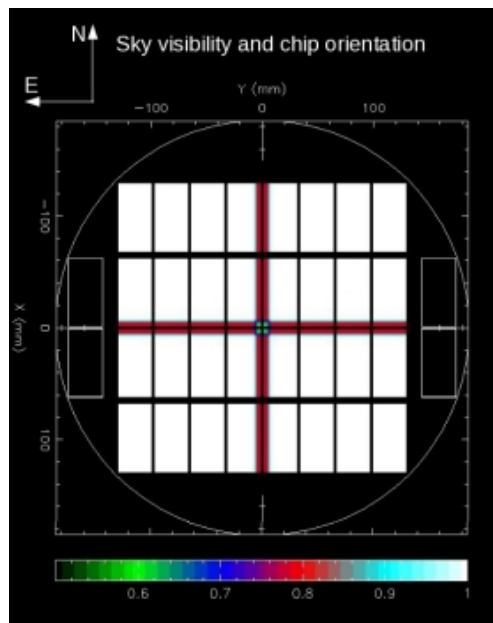


Figure 2.3: The scientific detector array of OmegaCAM with the central cross depicting the region vignettted by the quadrant structure of the H α filter. Source: ESO.

Table 2.1: The table lists the central wavelength (λ_0) and the effective width ($\Delta\lambda$) of the filters comprising our data-set. The exposure times for the deep exposures and the number of deep exposure observations along with the that for the short exposures are listed, too.

Filter	$\lambda_0/\Delta\lambda$ (nm)	λ range (nm)	Deep exp. (s)	# of Deep exp.	Shallow exp. (s)	# of Shallow exp.
u	350 / 60	320 - 380	300	53	10	9
g	480 / 140	410 - 550	120	19	5	17
r	625 / 140	555 - 695	90	38	2	17
i	770 / 150	695 - 845	90	16	3	17
z	910 / 120	850 - 970	75	8	-	0
H α	659 / 10	654 - 664	120	37	10	17

senting a wide central cross. This cross covers $310''$ in both X and Y direction vignetting the images (see Figure 2.3) and the jitter pattern is not enough to completely observe the region obscured by the central cross in H α filter. A *dithering* pattern would have made it possible to observe this region better. However, the data used for this thesis has been obtained as a part of a bigger program which focuses on variability of stars. Using a dither pattern would have led to the cluster's core region being observed from different CCDs in different epochs. This would have increased the dependence of our observations on the systematics of the telescope further.

The Table 2.1 reports the dataset in terms of the exposure times used for different filters and the number of observations in each one of them. The strategy established was to observe with two types of exposures in each filter: a deep and a shallow exposure. Deep and shallow exposure images were used to complement each other. The stars that might be saturated in the deep exposures could be retained in the shallow exposures. On the other hand, all the stars too faint to be observed in the shallow exposures were properly observed in the deep ones.

The exposure time used in any particular filter was set up while keeping in mind the spectral properties of NGC 6752 and the throughput curves of the filter. Since, a globular cluster holds an old stellar population, the exposure times in r band were set comparatively shorter than those in the u band. As the sensitivity of the u band (see Figure 2.2) is lower than the other bands and relatively fewer stars are expected to show substantial emission in this wavelength range, the exposure time for deep images was set up as 300 seconds.

The data was downloaded from ESO's image archive in FITS files compressed in the FZ format described in [Pence et al. \(2010\)](#). The FZ files were unpacked using FUNPACK. The

data extraction system from ESO has been set up in such a way to maximize scientific observation time and optimize the time spent in obtaining calibration images. The bias frames and flat fields are obtained regularly during an observation night. Whenever a science frame is asked for from the ESO archive, multiple biases and flats obtained in the same filter as the science frame are associated to the image.

Each set of images (the Data Block) consisted of the main science image in which the object (NGC 6752) was observed, along with the calibration images. The calibration images were typically comprised of 10 bias images taken before the science observation, 10 biases taken after the observation, and 5 flat-fields. Additionally, each set contained an XML file which helped in categorizing the images. The Data Blocks were then sorted as per the filter that was used while observing the images. These were then reduced independently according to the strategies discussed in the next section.

2.3 REDUCTION

The reduction of such a comprehensive data-set necessitated the use of a reduction pipeline capable of dealing with multi-wavelength, multi-chip observations. Bearing this in mind, ESO's Multi-Resolution Vision Model (MVM), also called *ALAMBIC*, was used for reducing the data.

2.3.1 ALAMBIC

ALAMBIC is an image reduction system - developed by Benoit Vandame (Vandame, 2002) - written in C++ which produces a platform-independent performance. The various techniques used in reduction (discussed below) are wrapped by employing the Extensible Markup Language (XML) technology. XML is used to take input of various parameters as a way of communicating between the modules and to maintain an internal database for all the tasks. By being an independent collection of libraries, the program avoids unnecessary access to disk and the entire reduction is carried out in memory, thereby enhancing the data rate of the process significantly. This is of paramount importance when dealing with a data-set like ours which occupies terabytes in disk space.

For preparation of the reduction, *Alambic* first reads the FITS header of images to garner information about the observations. It also reads the XML file present in each Data Block (DB) to categorize the data. Next, it asks for information about OmegaCAM: the number

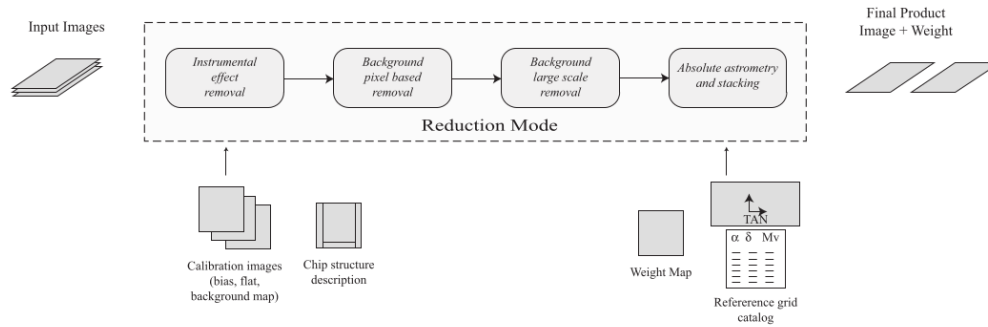


Figure 2.4: Flowchart portraying various steps used in reducing the data by Alambic. In the reduction mode used by us (Stellar), Alambic did not estimate or remove the background. Source: [Vandame \(2002\)](#).

of CCDs, their geometric layout, the electronic layout of each CCD, and the read-out noise and gain of different read-out ports. Keeping in mind the crowded nature of the field, the reduction mode was set as *stellar*. This mode doesn't try to estimate or remove the sky background, which can be varying significantly in a crowded globular cluster field. For details about various reduction modes, see [Vandame \(2004\)](#).

Alambic was originally designed for the ESO Imaging Survey and during the development of the code, OmegaCAM@VST wasn't functional. We use a modified version of Alambic developed by Marco Gullieuszik for the survey program OmegaWINGS ([Gullieuszik et al., 2015](#)). The modified version uses the same algorithms defined in [Vandame \(2004\)](#). However, it revamps the hardware and software dependency of the original code to increase the speed manifolds. It also enables us to factor in the central vignetting cross of H α filter while reducing those images.

The essence of the various reduction techniques implemented have been discussed below considering one Data Block as an example. To refresh, each Data Block contains the following observation for the same filter: 20 bias frames, 5 flat fields, 1 science frame, and 1 XML file with the association of different frames.

1. Data Organisation:

Each observation's FITS file comprised of 32 extensions - one for each of the 32 chips of OmegaCAM. These are split into single extension files and then grouped according to their classification. This step results in 32 *observation blocks*, each containing single-extension FITS files of the science frames, biases, and flats. These observation blocks are divided into *calibration blocks* (containing the bias and flat images) and the *reduction blocks* (containing the science images).

2. Instrumental Effect Removal:

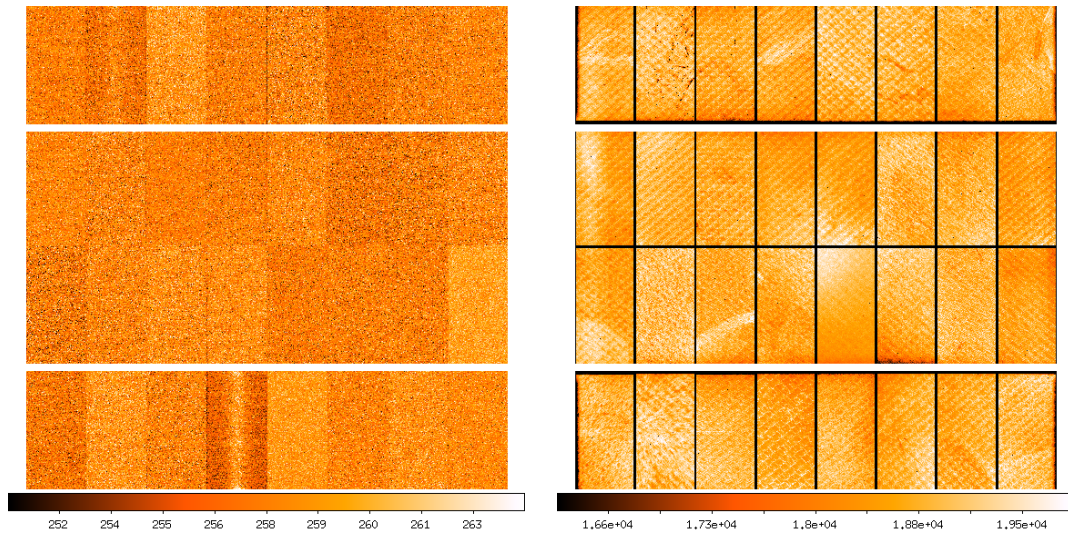


Figure 2.5: (Left) An example bias frame for a u-filter image. (Right) An example flat field for a u-filter image.

All the images in a single calibration block are stacked together (median combined) and the corresponding master bias and flat images are produced. Combining multiple frames to form a single master frame helps in removing cosmic ray hits and other instrumental effects. The master bias is overscan corrected before being subtracted from the science image and the flat fields are divided from the science frame.

This step is one of the fundamental steps in various reduction pipelines. However, Alambic specializes in the techniques described next. The code employs special algorithms for carrying out these pertinent processes.

3. Bad Pixel Masking and Weight Map:

The bad pixels on the CCD are identified in the master calibration images (bias and flats) and then a mask is created indicating these pixels which won't contribute to the final reduced images. This mask is multiplied with the master flat to produce the weight map, which characterizes the relative noise amplitude of the pixels.

4. Gain Harmonization:

The electronic converters of OmegaCAM's chips are not identical and showcase a 0.1% scatter in zero-points due to different gain for each chip. This results in a substantial difference between the mean sky background values (in ADUs) as measured in different chips. It is imperative to correct for this effect before applying the illumination maps to the flat images.

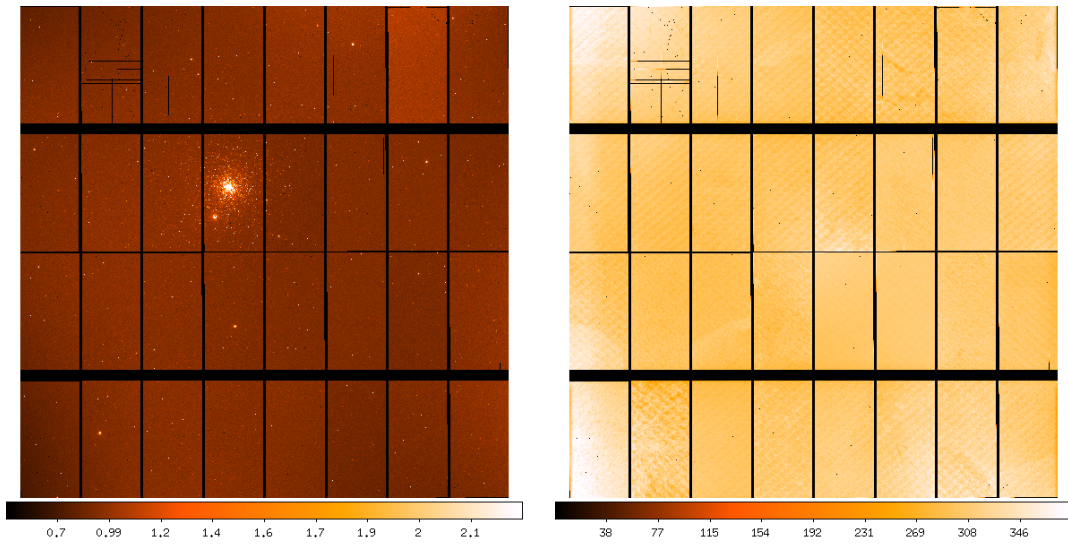


Figure 2.6: (Left) A u-filter raw image (Right) Weight map of the same image generated by Alambic using the above flat-field.

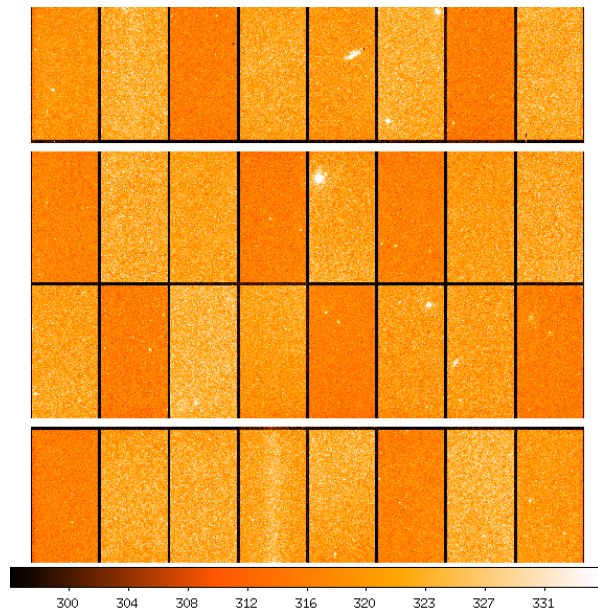


Figure 2.7: A u-filter standard field. These observations are taken regularly by ESO for quality control. The standard fields were used to harmonize the gain of the 32 OmegaCAM chips.

To harmonize the gain over all CCDs, chip 8 was chosen as the reference CCD, since it wasn't too crowded by the cluster but was close enough to the centre to encounter sufficient photons. The sky background level was calculated for 32 chips using a standard image and was normalized to the value of chip 8. These normalization coeffi-

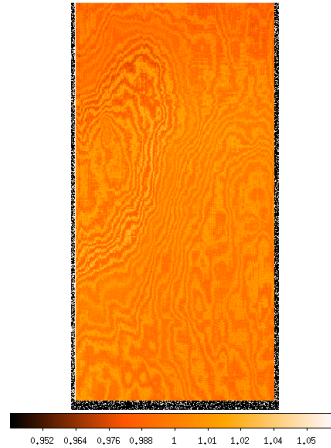


Figure 2.8: Chip 12's fringing map produced for the i-filter by median combining over 200 i-filter images.

cients were then multiplied to the calibration images for harmonizing the gain. A similar-epoch image observing a standard field - which is also used for the calibration of photometric zero-points - was downloaded for each filter. This observation was used as an external reference to normalize the background in other images.

5. Fringing Maps:

Fringes were observed in our data-set's band images which are caused due to the thickness of the CCD. They can also stem from sky emission lines, making a non-negligible contribution to the total signal, typically of the order of 10% of the background level. Fringing maps for the i band were obtained using more than 200 images with different pointings. These images were median-combined to obtain the final map bereft of any stars. These maps were used to de-fringe the observations before the final stacking of the science images.

6. Illumination Correction:

One of the main causes of photometric errors is the parasitic light added due to internal reflections off the telescope. The relatively open VST dome facilitates in improving seeing by allowing air to pass through it. However, this also leads to increased scattered light which impairs flat-fielding. This error results in a star of same brightness showing different flux if observed in different positions on the CCD. The net result, when flat-field exposures are applied without any correction, is an erroneous apparent trend of photometric zero-point as a function of the distance from the centre of the camera's field of view. To correct this effect, an illumination map measuring relative flux error is computed and then used to correct the master flats. This helps in avoiding propagation of the illumination error to the science image.

The illumination map was computed for each filter using multiple images observed with a dithering pattern. These images were reduced using the normal calibration im-

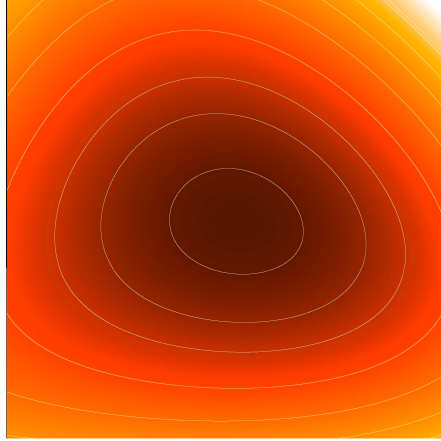


Figure 2.9: Illumination map produced for the u-filter using 12 dithered observations of the Landolt Selected Area 113.

ages and the same algorithms discussed here. Photometric catalogs were created for individual images and then compared. Since each star will be placed at a different position in each image, the zero-point variations were mapped as a function of the position on the focal plane. This was done using a least square estimator approximating the illumination map with a n-D polynomial function. The polynomial order for the u filter’s illumination map was computed to be 4 while for the rest of the filters a 3rd order polynomial produced the best illumination map. The illumination map for the u filters is shown in Figure 2.9. The maps produced by us are in good agreement with the ones produced by the VPHAS group (Drew et al., 2014).

7. Astrometry and Stacking:

The last module of the reduction process is responsible for producing a final image which combines all the images in the reduction block, normalized to one second integration time and astrometrically calibrating the final image. The Gaia DR2 catalog (Gaia Collaboration et al., 2018) was used as a reference catalog for astrometric calibration. The astrometric solution was found using a wavelet decomposition method as described in Vandame (2004).

These steps were carried out independently for all Data Blocks. An average run of all these steps for a single Data Block took 5 minutes on a 48-core machine. The final reduced science image was then multiplied by its exposure time as Alambic normalizes it to a 1-second exposure image. All such images and their corresponding weights were then treated separately for their photometric extraction using a combination of SExtractor and DAOPHOT as explained in the next chapter.

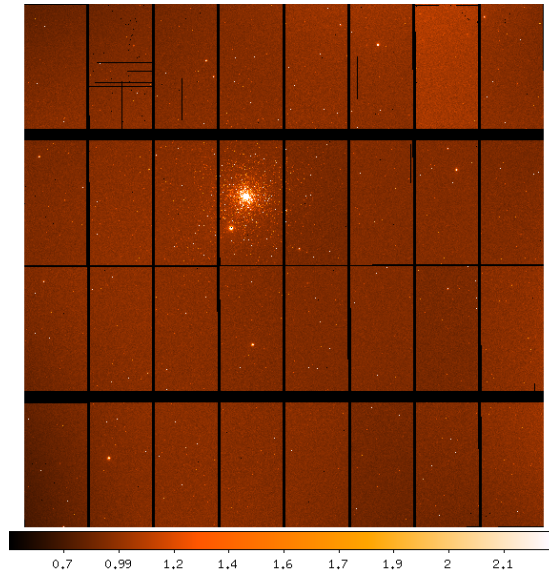


Figure 2.10: The final science frame produced by Alambic by reducing the raw and calibration frames shown in Figures 2.5, 2.6. The cluster's centre is located in Chip 12 of the CCD array.

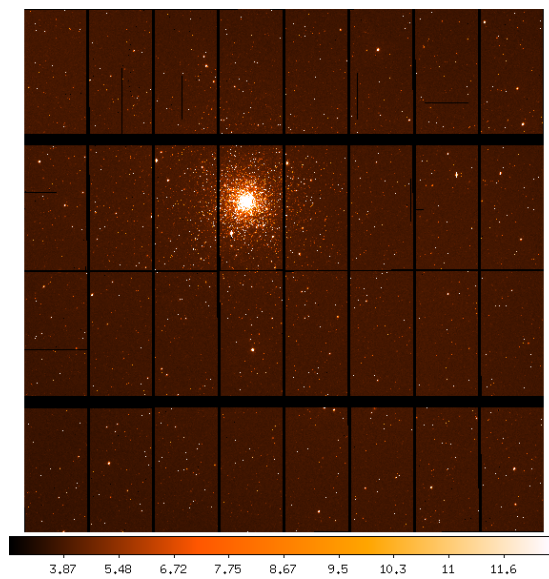


Figure 2.11: Similarly reduced i-filter science frame produced by Alambic. The raw i-filter frames were de-fringed using the fringing maps displayed in 2.8. In comparison to Figure 2.10, this image contains significantly more stars due to the older stellar population of NGC 6752.

Initial Product:

Raw images in all the filters.

End Product:

Reduced images ready for photometric extraction.

If there is anything that can bind the heavenly mind of man to this dreary exile of our earthly home and can reconcile us with our fate so that one can enjoy living, then it is verily the enjoyment of the mathematical sciences and astronomy.

Johannes Kepler

3

Photometry

After the raw images in all the filters had been reduced, the science frames were ready for photometric extraction. The aim was to get a multi-band deep catalog of all the stars in the 1×1 degree² field of view. In order to robustly compute instrumental magnitudes of all the stars, Peter Stetson's DAOPHOT II software suite was used to perform PSF photometry (Stetson, 1987).

DAOPHOT has been designed to function in an interactive way, which would be impractical to perform for our data-set given the large number of images at our disposal. A substantial amount of time was invested in developing a fully automatized procedure for extracting DAOPHOT photometry in an unsupervised manner. The procedure employed several algorithms to satisfy DAOPHOT's requirements. For example, one prerequisite for DAOPHOT is the full-width at half-maximum (FWHM) of unresolved stellar objects in the frame. In order to calculate the FWHM of such a large number of images, an automatic routine was developed which used Source Extractor (Bertin & Arnouts, 1996) to calculate the FWHM. Along with the FWHM, a whole host of other information regarding the OmegaCAM CCDs was provided, viz. the gain (in e-/ADU), the readout noise per pixel (in e-), the saturation level of images (in ADU). The entire procedure for extracting the photometry was developed in Python.

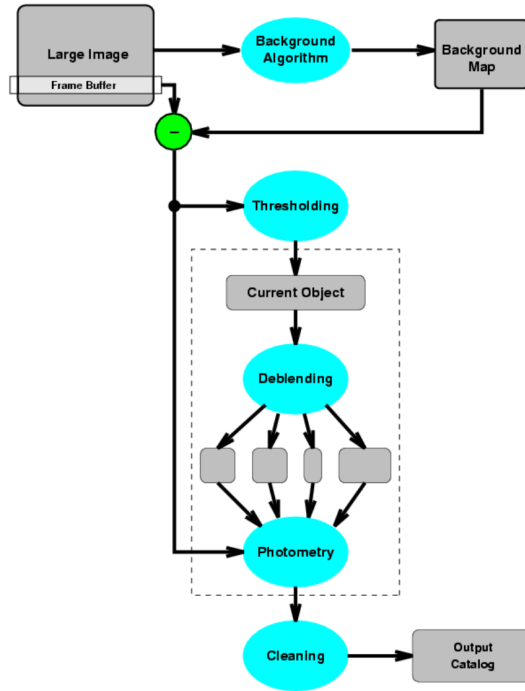


Figure 3.1: Flowchart depicting the procedures involved in the 1st run of SExtractor. The program first models the background and detects regions with sufficient flux over a user-defined threshold. It deblends these regions and performs aperture photometry. In the last step it cleans the catalog based on various filtering parameters. Source: SExtractor user manual.

3.1 SOURCE EXTRACTOR

Source Extractor (SEXTRACTOR, Bertin & Arnouts (1996)) is a software that extracts all the sources in an image and generates their catalogue. Loosely, SEXTRACTOR first models the sky background and subtracts it from the image (see Fig. 3.1). It then filters the image by convolving it with a Gaussian kernel to lower the effect of noise in the image. Then all the pixel regions in which a significant flux over a threshold level is observed are considered as detections. These detections are then resolved and aperture photometry is performed on them. The sources are then classified as either stars or galaxies using a neural network and the magnitude and other physical parameters related to the shape of the sources are transferred to the catalog. For a detailed description of SEXTRACTOR, see the official user’s manual from the developers* and also another excellent guide for beginners†.

*<https://www.astromatic.net/pubsvn/software/sextractor/trunk/doc/sextractor.pdf>

†http://astroa.physics.metu.edu.tr/MANUALS/sextractor/Guide2source_extractor.pdf

A routine was developed in Python to run `SEXTRACTOR` on all images of the data-set and calculate the FWHM in two steps. In the output catalogs generated by a single run of `SEXTRACTOR`, the FWHM of each detected source along with the results of aperture photometry were present. Only those sources with the quality parameter $FLAG = 0$ (c.f. the user manual) were considered for computing the FWHM in both the steps.

In the first step, no weight map was provided to `SEXTRACTOR` and the default Gaussian kernel was used for smoothing the image. Once the catalog of extracted sources is generated, the FWHM vector is iteratively clipped at $\pm 2\sigma$ about its median till convergence. In the second step, the mean of this sigma-clipped vector is used to create a custom Gaussian kernel which is provided to `SEXTRACTOR` for filtering the image by using it as a convolution operator. The approximately-Gaussian PSF cores of really low brightness stars can be detected in a better manner after convolution.

Additionally, the weight map generated for each image by `Alambic` during the reduction process (see Section 2.3.1) is provided to `SEXTRACTOR` to get a better estimate of the background and noise in the image. Including weight maps in its process, `SEXTRACTOR` can produce error estimates more accurately. With the 2 additions in the second step - (i) the custom Gaussian smoothing kernel and (ii) the weight map - the output catalog generated in this step was used to derive the FWHM. As done in the first step, the FWHM vector of the catalog was iteratively clipped and the mean was accepted as the best estimate of FWHM. This final FWHM, in pixels, was fed to `DAOPHOT` through its option files.

3.2 DAOPHOT II

Saying `DAOPHOT` is widely used in Astronomy would be an understatement - as is underlined by the fact that the original paper [Stetson \(1987\)](#) has been cited more than 5000 times. A Python routine was developed to use `DAOPHOT` for performing photometry and also filter the files created by `DAOPHOT`'s tasks before feeding them to its subsequent routines.

After getting the FWHM, other parameters - like the fitting radius, PSF radius - pertinent to a successful photometry were calculated as a function of the FWHM. For details on the various radii, refer the official manual[‡]. With the various radii defined, `DAOPHOT`'s `FIND` task was used to find the coordinates of all possible stars in the field and `PHOTOMETRY` was used to perform aperture photometry. The routine used to run `DAOPHOT` is described

[‡]<http://www.astro.wisc.edu/sirtf/daophot2.pdf>

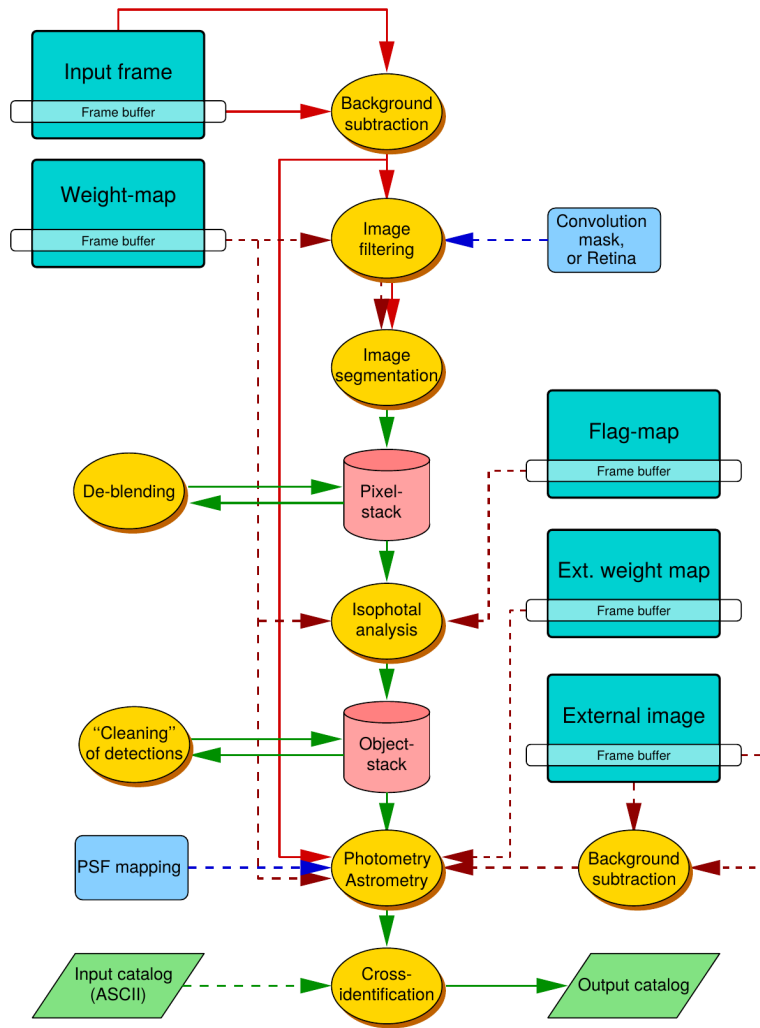


Figure 3.2: Many of the principles described here are employed in the 2nd run of SExtractor. The weight map produced for each image by Alambic was fed to SExtractor. Using the FWHM calculated in the first step, a new Gaussian convolution mask was created and given to the program. Source: SExtractor user manual.

here keeping just one image in mind. This procedure was executed in the same way for the entire data-set.

Once the aperture photometry file was ready, the list of stars was sorted in ascending order of magnitude and the brightest stars (likely to be saturated) were ignored while selecting the PSF stars. In DAOPHOT's PICK command, 200 relatively bright, spread out, and isolated stars were selected to model the PSF. The PSF command was used iteratively till no star with any source of contamination from a neighbour was selected. The selection of the PSF model was set to auto mode which means DAOPHOT tried to model the PSF with the mathematical functions stored in its library (Gaussian, Lorentz, Moffat, etc.) and it chose the best fitting function automatically.

After the PSF of the image was created and its aperture photometry was performed, the files were fed to ALLSTAR to perform PSF photometry. ALLSTAR uses an analytical PSF along with the empirical one while fitting the star's profile. The star-subtracted images which contain the residuals of PSF modeling were inspected to refine the various fitting radii. The photometry file generated by ALLSTAR contains the co-ordinates (in physical units) and PSF-fitted instrumental magnitudes of the stars detected in the image. Such files were obtained for the entire data-set by running DAOPHOT and ALLSTAR. In order to fix the position and calculate the magnitude of the stars with greater precision, all the photometry files were matched to create a master catalogue using DAOMATCH and DAOMASTER.

3.3 DAOMATCH & DAOMASTER

As shown in Table 2.1, the data-set consisted of multiple images with the same exposure times observed in the same filter. In order to extract maximum information from these images and to generate a deeper catalog, the independently reduced single images were matched frame by frame using DAOMATCH. As the data-set was obtained employing a small jitter pattern, it was imperative to use DAOMATCH to calculate the transformation coefficients between the master frame and the others. The master frame for each filter (and each exposure time) was selected as the image with the best seeing (lowest FWHM) as calculated by the PSF task in DAOPHOT. This was invariably the same frame which had most number of stars detected and *photometrized*.

DAOMATCH Stetson (1993) uses a triangle matching algorithm and a user-defined transformation function for finding the shifts between the frames. Once the transformation coefficients with respect to the master frame were computed, DAOMASTER was used to shift

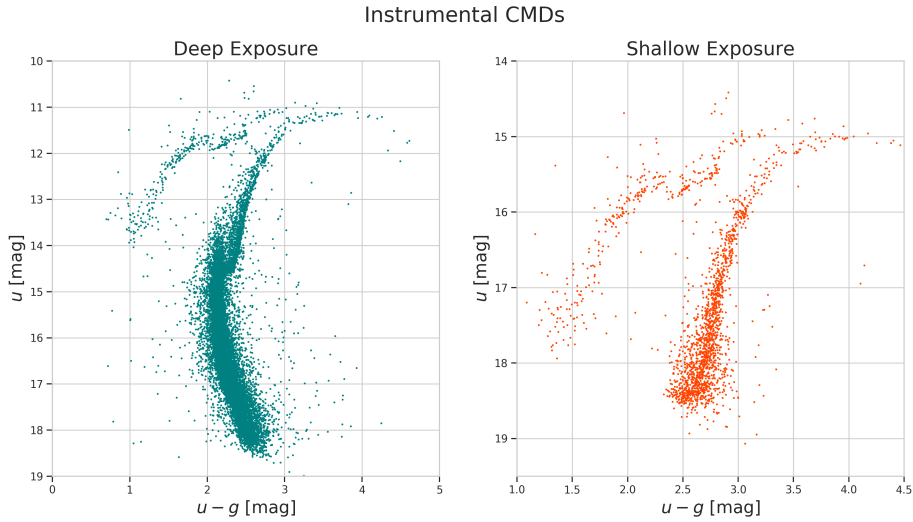


Figure 3.3: Instrumental u vs $u-g$ CMD. As the magnitudes are not calibrated in this plot, the horizontal branch magnitude in both the exposures is significantly different. The zero-point used by daophot is 25.0. Instrumental magnitudes are assigned with respect to the faintest star (above the background level) detected in an image. As the background level is different in deep and short exposures, the instrumental magnitudes of the same star in these exposures can be significantly offset.

the coordinates of the stars detected in each frame to the coordinates of the same stars in the master frame. It assigns a final magnitude to each star based on a robust average of the star's magnitude calculated in the frames in which it was detected. It also computes a variability index using the magnitudes and errors computed for each single frame.

The final magnitude file generated by DAOMASTER is the catalog of all the stars detected in the majority of the images of a single filter for a particular exposure time. These catalogs were matched pairwise for various filters (and for deep and shallow exposures) to generate a color-magnitude diagram based on instrumental measurements (un-calibrated magnitudes). For example, the catalog generated for u filter's deep exposures was matched with the catalog created for g filter's deep exposures using the same routines described above.

The master frame for DAOMATCH was decided based on the leading magnitude in the color magnitude diagrams (CMDs). In the u , $(u-g)$ CMD, u filter's catalog was chosen as the master frame. The co-ordinates of stars in the g catalog were shifted to those of the stars in the u catalog. DAOMASTER was set up in such a way that all the stars present in one filter but not the other were included in the final catalog, too. For the stars present in both the catalogs, both the magnitudes were taken as-is without doing the physically meaningless averaging of magnitudes calculated for two different filters.

After the matching, several test images were produced to check the quality of the photometry. For every filter, several of these images were checked to refine the various parameters involved in the process. The instrumental CMD for the pair-wise filters (u vs g, r vs i, etc.) was produced. We also produced tables tracking the magnitude of all the stars in each frame for both the filters useful for producing light curves.

Once these preliminary checks were completed, the code was run on the entire data-set. After the master catalog with final instrumental magnitude of all the stars observed in a given exposure time and a given filter was generated, aperture correction and zero-point calibration were performed.

3.4 APERTURE CORRECTION

When performing PSF photometry, it is important to correct the profile-fitted magnitudes for flux-loss to recover the true magnitude of the stars. It is not practically possible to measure the entire flux of the star as it gets spread over a large area of the CCD. The PSF model, for e.g. the Gaussian, is usually clipped at 3 - 4 sigmas and the flux beyond this point is assumed to be zero. In order to recover this flux and garner better signal-to-noise ratio, aperture correction is performed.

To compute the value of aperture correction, brightest objects along the Red Giant Branch in the CMD were selected. These stars were then located in both the filters' (for e.g. the u and g filters in the u, (u-g), CMD) master magnitude file by using the transfer file created by DAOMASTER. Aperture photometry was carried out by implementing the same routine described in Section 3.2 with only one change: 12 increasing aperture sizes were given in the photometry option file to get 12 different magnitudes.

A set of maximum 100 stars was selected from each chip and photometrised. This photometry was performed on the best-seeing image which was given to DAOMATCH as the master frame; whose co-ordinates and magnitudes were used as reference by DAOMASTER. The newly calculated 12 aperture magnitudes of all these stars were then subtracted from the PSF magnitude of these stars computed by DAOMASTER. This difference in magnitude of all the stars (Δ_{mag}) was plotted against the aperture size as shown in Figure 3.4 and a 3-sigma clipped median of these differences was computed to produce the growth curve (right panel of Figure 3.4).

The right part of the growth curve at which it stagnates gives the best estimate of the aperture correction. A median of the last 5 values of the growth curve was accepted as the

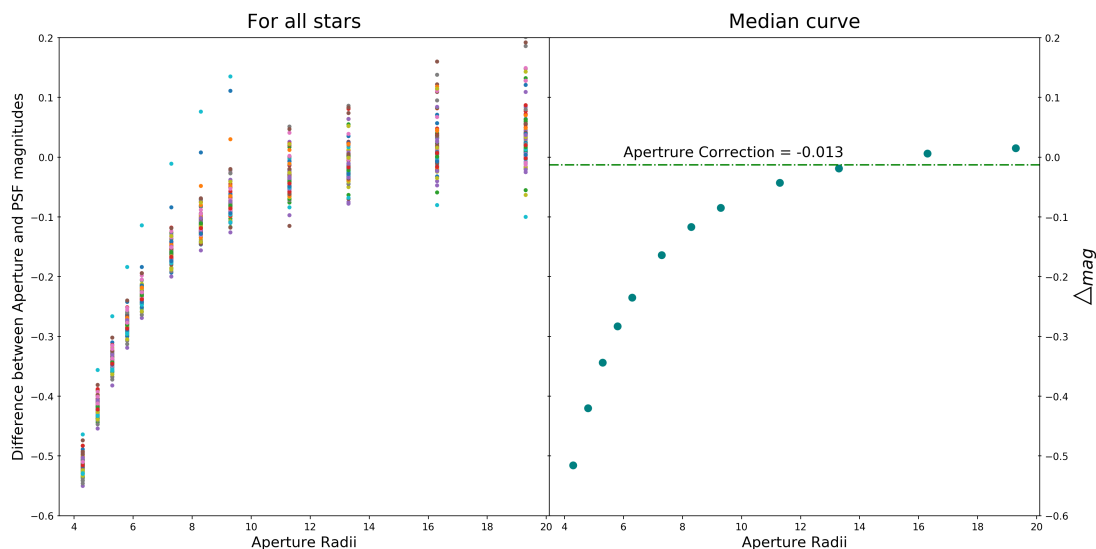


Figure 3.4: Δ_{mag} is the difference between the allstar-calculated PSF magnitudes and the 12 aperture magnitudes. (Left) Growth curves for the bright stars selected from u, (u-g) CMD produced for Chip 10. (Right) The median growth curve was used to calculate the final value for aperture correction.

aperture correction for that particular chip in that particular filter. This was repeated for the entire data-set and these aperture corrections were then subtracted from the PSF magnitude of the stars to derive the *total* instrumental magnitude of the stars.

3.5 CALIBRATION

Calibration of the instrumental magnitudes can be carried out in two ways. In the traditional method, standard fields are observed, photometrised, and their instrumental magnitudes are transformed to their published values. These transformation equations are then used to calibrate the instrumental magnitude of all the stars. In the other method, which we used, photometric zero-points for the CCDs are obtained and already published values of the stars are used to transform the instrumental values to the photometric system of the published values. The steps involved in our calibration are elaborated below:

1. Photometric zero-point

DAOPHOT computes instrumental magnitudes assuming a photometric zero-point of 25.0 mag. However, every CCD chip in every filter exhibits a different zero-point. As explained in Section 2.3.1, CCD 8 was used as the chip for gain harmonization of the CCDs. Therefore, the photometric zero-point of OmegaCAM's CCD 8 in all filters

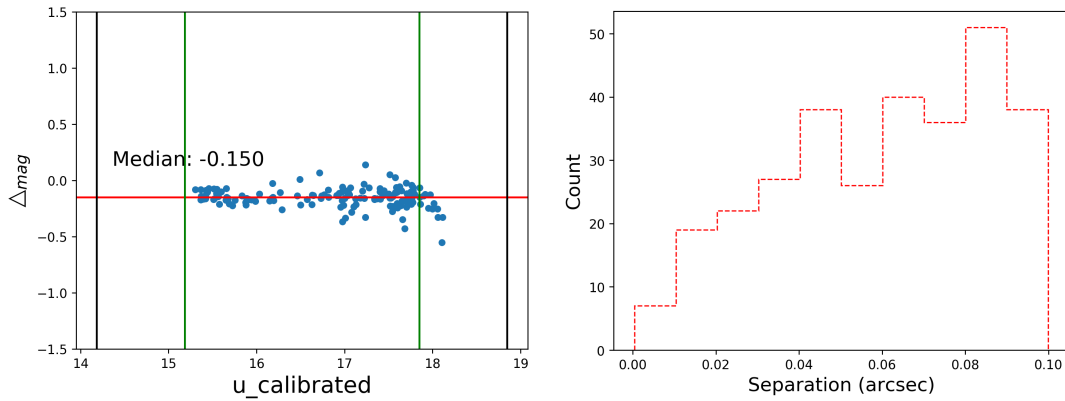


Figure 3.5: (Left) Δ_{mag} on the Y-axis is the difference between the calibrated magnitude of our data and the magnitude calculated by SkyMapper. The plot shows Δ_{mag} as a function of our calibrated u-magnitude for stars in Chip 10. While matching our photometry with SkyMapper’s, a separation distance of 0.1 arcseconds was used. This ensured no spurious matches crept into our data. The value for Δ_{mag} is consistent throughout the magnitude range and scatters a bit towards the fainter magnitudes. The green lines represent a 2-sigma cut-off region and the black lines are placed at one magnitude farther from the cut-off region. Only the stars within the cut-off region are used to calculate the median value of Δ_{mag} which is shown by the red line. (Right) A histogram of the separation distance between the matched stars in our and SkyMapper’s photometry. Only the stars that were found with 0.1 arcseconds of each other were considered as true matches.

was obtained from ESO’s quality control (QC) database[§].

In order to account for the shifts in zero-point over the course of our observations, the database was queried to provide zero-points for all observing epochs. The zero-points extracted for CCD 8 were those calculated by ESO’s QC group using the same exposure times as the ones in our data-set. These zero-points were added to the instrumental magnitudes after the subtraction of the DAOPHOT-induced default value of 25.0 mag.

2. Atmospheric Corrections

For converting instrumental magnitudes to extra-atmosphere instrumental magnitudes, one has to correct for atmospheric extinction and airmass. Extinction coefficient in each filter was obtained from ESO’s QC database while airmass was extracted from the header of the reference image’s FITS file. Their product was subtracted from the magnitudes as these lead to a loss in flux of the star, i.e. a larger magnitude.

3. Normalizing Exposure

The magnitudes in deep and shallow exposures cannot be combined directly and therefore, it is necessary to normalize them to a 1-second exposure before comparing or combining them. Therefore, the normalizing term $2.5 \log_{10}(\text{Exposure Time})$ was added to the instrumental magnitudes.

[§]http://archive.eso.org/qc1/qc1.cgi?action=qc1_browse_instrume&instrume=OMEGACAM

4. SkyMapper

SkyMapper is a 1.3-meter telescope at Siding Spring Observatory, Australia, observing the entire southern hemisphere in the Sloan ugriz filters (Wolf et al., 2018). The throughput curves of these filters resemble those of the OmegaCAM's filters very closely. Therefore, in the final calibration step, we compared our photometry with theirs to remove any zero-point inhomogeneities lurking on a chip-to-chip level.

The SkyMapper DR2 database was queried using Astronomy Data Query Language (ADQL) via Virtual Observatory's Table Access Protocol (TAP). A 1×1 degree² region around the cluster's centre was queried and all the stars which satisfied the following constraints were selected:

- flag = 0
- nimaflag = 0
- ngood > 1

These restrictions ensured the reliability of the selected stars' photometry[‡]. The stars in our catalog were matched against the stars in SkyMapper DR2 on a chip-to-chip basis. A sigma-clipped median (as seen in Figure 3.5) of the differences in the magnitudes of the matched stars was taken as the zero-point offset between the 2 photometries. These zero-points were added to the computed magnitudes to shift them to the SkyMapper photometric system.

These varied corrections were incorporated for the entire data-set and the final calibrated magnitude of all the stars was obtained. However, it is important to note that these magnitudes have been calculated for single-chip, single-exposure, and single-filter catalogs. For example, these calibrated magnitudes are present in 32 single-CCD files for the deep exposures of the u-filter data. The next chapter emphasizes on how these independent photometries were combined to produce the final master catalog of the entire data-set.

Initial product:

Reduced images ready for photometric extraction.

End Product:

Single-chip, single-exposure, single-filter catalogs containing final calibrated magnitude of all the stars with their photometric errors and variability index.

[‡]For details of these parameters, please refer the SkyMapper Table metadata: <http://skymapper.anu.edu.au/table-browser/>

Philosophy is written in this grand book, the universe, which stands continually open to our gaze. But the book cannot be understood unless one first learns to comprehend the language and read the letters in which it is composed. It is written in the language of mathematics, and its characters are triangles, circles, and other geometric figures without which it is humanly impossible to understand a single word of it; without these, one wanders about in a dark labyrinth.

Galileo Galilei

4

The Catalog

The independently photometrised plethora of catalogs had to be woven together meticulously to produce a single master catalog. In essence, the 32-CCD catalogs of a single exposure were stitched together one-by-one, the shallow and deep exposures were matched selectively, these single-filter catalogs were then matched against each other to generate the final catalog with more than 140,000 stars. This catalog was joined with multiple other surveys to provide magnitudes throughout the spectral energy distribution of the cluster. This chapter elaborates each of these steps descriptively.

4.1 STITCHING

As explained in Section 2.2, a jitter pattern was used to cover the vertical gaps in OmegaCAM's CCDs. This jitter pattern results in the same star being observed from 2 or 3 different CCDs over the entire epoch of observations. Therefore, it is important to treat these duplicates before combining the catalogs. A Python routine was developed to overcome these inconsistencies by stitching the CCD chips one by one.

The 8 CCDs along a single row of OmegaCAM's CCD array (shown in Figure 4.1) were matched with their immediate neighbour. The magnitude of any star found in the overlapping regions of 2 adjacent CCDs was taken as a weighted average of its measurements in both of them. The number of images in which it was found in a particular CCD was used as the weight in averaging. This was repeated for all 4 rows of the CCD array and the middle 2 rows

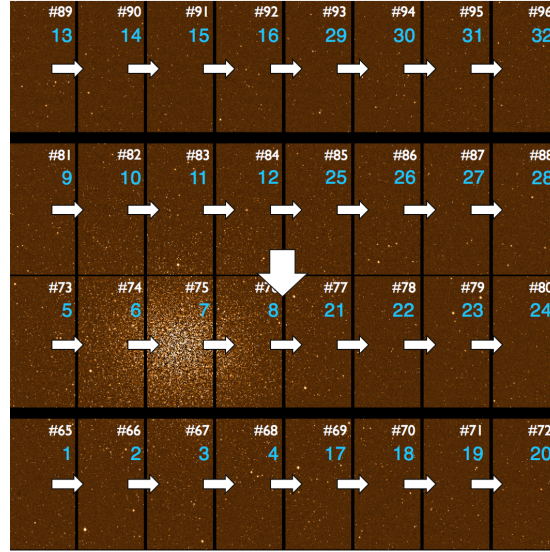


Figure 4.1: The numbers on individual chips represent ESO nomenclature for the CCD. For removing duplicates present due to the horizontal component of the jitter pattern, the adjacent CCDs were matched. For e.g., Chip 1 was matched with 2 and their combined catalog was matched with Chip 3. This was repeated for all 4 rows. The middle 2 rows (Row 5-24 and Row 9-28) were matched to account for the matches emerging due to the vertical component of the jitter. As the horizontal gaps between Row 13-32 and Row 9-28 is $85''$ the jitter pattern did not result in any overlap in this region.

were then matched against each other to recover those duplicates arising due to the vertical component of the jitter.

Once all these repeated measurements were averaged, an integrated catalog of all CCDs for a single exposure type and a single filter was ready. The next step was to combine the deep and shallow exposure catalogs.

4.2 COMBINING DEEP-SHALLOW

The exposure times in various filters were set up to recover both the faint stars undetectable in shallow exposures and the bright stars saturated in the deep exposure. In order to exploit the advantage of bearing these different kinds of exposures, their catalogs were matched intricately.

A k-d tree algorithm (Bentley, 1975) was implemented to find the matches between the 2 catalogs. Out of all the matches, a level of magnitude was derived for each filter above which only the shallow-exposure magnitude was kept for the matched stars. Whereas, for all the duplicates below this saturation boundary, only their deep-exposure magnitude was accepted. All the stars in shallow-exposure catalog above this magnitude-level, which did not

find a match in the deep exposures were also included in the combined ensemble.

This combined catalog was checked again for duplicates or triplicates that might have been missed previously. A Python routine for internal matching of the tables was developed which used $0''.1$ as an accepted tolerance level. Any pair of stars in which the stars are separated by less than $0''.1$ were examined for their magnitudes and the number of frames they were detected in. In the very few of such cases (~ 20 stars in the r-filter) where these close stars had almost similar magnitudes, only the measurement with more number of detections was incorporated into the combined catalog.

We refrained from combining magnitudes derived for two different kinds of exposure times (even after normalizing them to a 1-second exposure) and therefore, the aforementioned painstaking matching was performed. The step was repeated for all the filters except for the z-filter as there were no short-exposure images observed in it.

4.3 COMBINING FILTERS

This was the final step in generating the master catalog produced from the photometry of our own data-set. The mainly reddish, old stellar population of NGC 6752 is particularly prominent in the r-filter and the shallow+deep exposure catalog of this band consisted of 140,000+ stars. Therefore, r-filter's catalog was used as the reference for the amalgamation of the data-set.

The result of the matches between the r-filter and other filters' catalogs is summarized in Table 4.1. During the matching, the difference in RA and DEC was plotted for all the linked stars and their 2-d separation (in arcseconds) was plotted as a function of their magnitude. These plots for the matches between the *r* and *i* catalogs are shown in the lower and upper panels of Figure 4.2, respectively.

By studying the distribution of points in these plots, it was possible to refine the maximum separation considered for a true match. For the matches, the mean separation distance (μ , its uncertainty) and its standard deviation (σ) were:

$$\begin{aligned}\mu &= 0.0354 \pm 0.0001 \text{ arcsec} \\ \sigma &= 0.0282 \text{ arcsec}\end{aligned}\tag{4.1}$$

Since, the astrometry of the data-set was done consistently, a stringent value of $0''.2$ was accepted for these internal matches. Any star in r-filter, which matched a star in any other

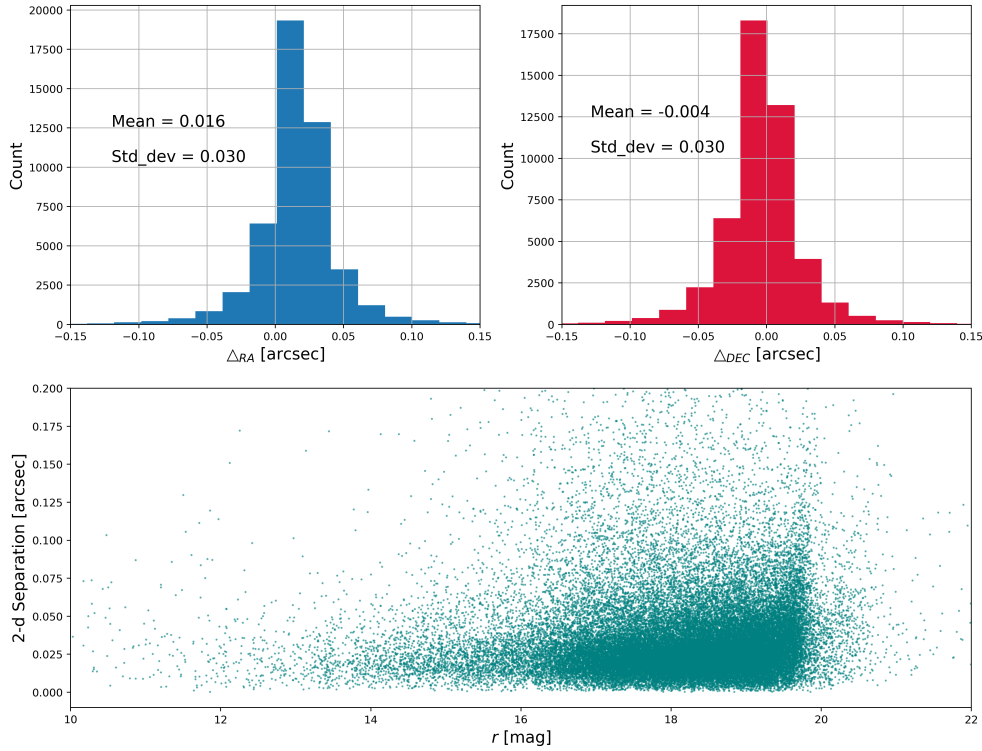


Figure 4.2: The top panels display histograms of Δ_{RA} and Δ_{DEC} . These are the difference between the position of the stars in the r- and u-filter catalogs in arcseconds. The mean and standard deviation for both of them are displayed in the plot. As can be seen easily, majority of the stars had very similar positions in both the catalogs; a testament of Omega-CAM’s stable pointing ability. The bottom panel displays the separation distance for the matched stars as a function of the r-filter magnitude. At approximately $r = 20$ mag, the separation distance scatters the most. The histograms as well as this plot reiterate that $0''.2$ is a suitable matching radius and no spurious matches are included.

filter with a separation of greater than $0''.2$ (approximately the pixel size), wasn’t considered as a successful match. The stars in the r-filter unmatched with other filters were incorporated into the final catalog, too. As a result, the final number of stars in this catalog was 141,633.

This concluded the procurement of the final master catalog of our data-set. The calibrated PSF-fitted magnitude, photometric errors, variability index, and other parameters pertaining to the star’s shape were the properties present for all the stars in each of the filters. Along with these, a flag parameter was computed for the stars detected in the $H\alpha$ filter. As explained earlier in the Chapter 2, this filter is made of 4 quadrants resulting in a vignetting central-cross. It was found that due to this feature, the photometry of stars present in this region showed significant difference with respect to other stars. Therefore, the flag parameter for stars situated within the central cross was set a value of 1, and for the rest of the population, it was set to 0. The CMDs of our data-set are shown in Figures 4.3 and 4.4.

Table 4.1: As the final catalogs of all the filters were matched against the r-filter's catalog. In each matching, all the stars from the r-filter observations were retained (an SQL left outer join was performed).

Filter	Number of stars	Number of matches with the <i>r</i> catalog
u	52327	46279
g	89545	86066
r	141633	-
i	119821	110050
z	59872	54080
H α	76013	71093

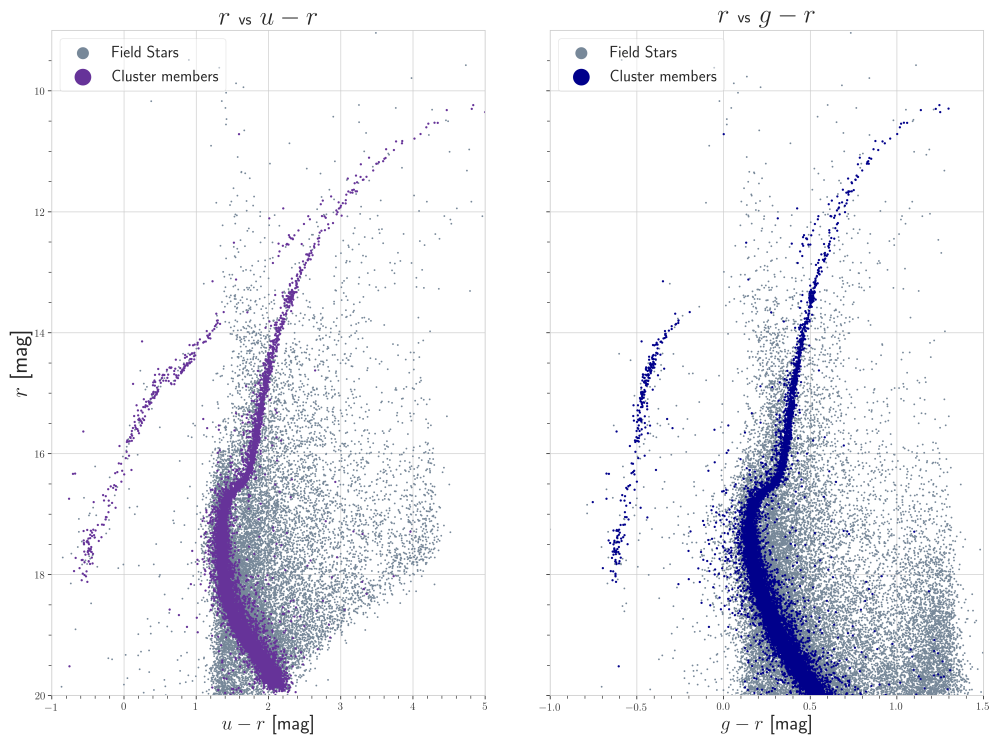


Figure 4.3: The calibrated color magnitude diagrams produced using *u*, *g*, *r* magnitudes and colors from the final master catalog of our photometrised data-set. Cluster members were provisionally selected as those within 18 arcminutes from the centre of the cluster and having a total proper motion of less than 1.5 mas/yr with respect to the centre of the cluster. This selection was performed for representational purposes only.

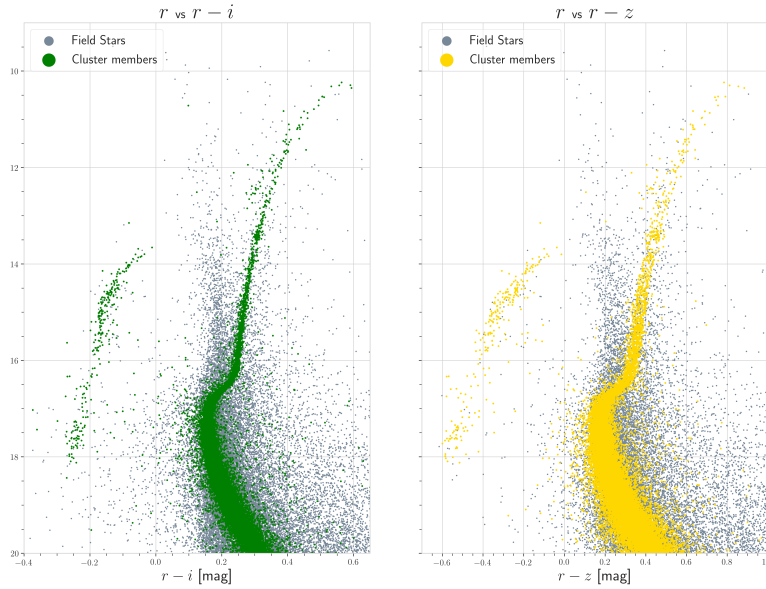


Figure 4.4: The calibrated color magnitude diagrams produced using r , i , z magnitudes and colors from the final master catalog of our photometrised data-set.

4.4 MATCHING EXTERNAL SURVEYS

In order to complement our multi-band coverage with existing all-sky surveys in different wavelength regions, we matched our catalog with those of the Gaia, 2MASS, WISE, and GALEX surveys. Additionally, we matched our catalog with the VHS and HUGS surveys, as NGC6752 has been observed extensively by them.

4.4.1 PROCURING THE CATALOGS

These catalogs were obtained using the *Simple Cone Search* service of Virtual Observatory accessed using the Python module *pyvo*. For each survey, a 1×1 degree² region around the cluster's centre was queried and matched against our catalog. The URLs used for the Cone Search of the surveys and the number of stars selected from them are shown in Table 4.2.

Each external match has been described in the following pages.

4.4.2 GAIA

As already explained in Section 2.3.1, Alambic used Gaia DR2 (Gaia Collaboration et al., 2018) as a reference grid for astrometric calibration of the images. Therefore, a stringent $0''.2$ distance was used in matching. The coordinates of the stars were then shifted to Gaia's

Table 4.2: List of surveys matched with our catalog. Each catalog was surveyed using the Simple Cone Search facility of pyvo. These surveys boosted the spectral coverage of the catalog.

Survey	# of matched stars	Cone Search link
Gaia DR2	77958	http://gaia.ari.uni-heidelberg.de/cone/search
Galaxy Evolution Explorer (GALEX)	6369	http://gsss.stsci.edu/webservices/vo/ConeSearch.aspx?CAT=GALEX&
Two Micron All-Sky Survey (2MASS)	11839	http://wfaudata.roe.ac.uk/twomass-dsa/DirectCone?DSACAT=TWOMASS&DSATAB=twomass_xsc&
VISTA Hemisphere Survey (VHS)	84916	http://wfaudata.roe.ac.uk/vhsDR6-dsa/DirectCone?DSACAT=VHS_DR6&DSATAB=vhsSource&
Wide-field Infrared Survey Explorer (WISE)	10757	http://gsss.stsci.edu/webservices/vo/ConeSearch.aspx?CAT=WISE&
HST UV Globular Cluster Survey (HUGS)	12287	https://archive.stsci.edu/hlsp/hugs/ngc6752/
Stetson Homogeneous Photometry	90828	https://www.canfar.net/storage/list/STETSON/homogeneous/MNRAS_Photometry_for_48_Clusters/NGC6752

reference epoch of 2015.5. Crucial information of the stars' astrometry like proper motion, parallax, radial velocity was obtained from Gaia and later used to establish the membership criterion. CMDs with Gaia magnitudes are presented in Figure 4.5.

4.4.3 GALEX

The catalog was matched with Galaxy Evolution Explorer (GALEX, [Martin et al. 2005](#)) survey to extend the catalog's UV coverage. The Near-Ultraviolet (NUV) and Far-Ultraviolet (FUV) magnitudes were incorporated to the catalog. As the resolution of GALEX is comparatively lower, a matching radius of $0''.5$ was chosen. Since the cluster harbors older stellar populations, only ~ 6300 stars were found to be common between GALEX and our catalog.

4.4.4 2MASS + VHS

To get the near-infrared photometric magnitudes of the stars, the catalog was matched against the Two Micron All-Sky Survey (2MASS, [Skrutskie et al. 2006](#)) and the VISTA Hemisphere Survey (VHS, [McMahon et al. 2013](#)). Their combination was used keeping in mind that all objects brighter than 14 mag in K band are saturated in VHS (due to the highly efficient CCDs) but could be recovered in 2MASS. However, VHS adds fainter stars to the catalog that are absent in 2MASS. In these matches, a maximum separation distance of 0.5 and 0.2 arcseconds was used for 2MASS and VHS, respectively. A larger separation distance was used for 2MASS as its astrometry is less accurate than that of ours. A CMD produced using a combination of K_{VHS} and K_{2MASS} is presented in Figure 4.6.

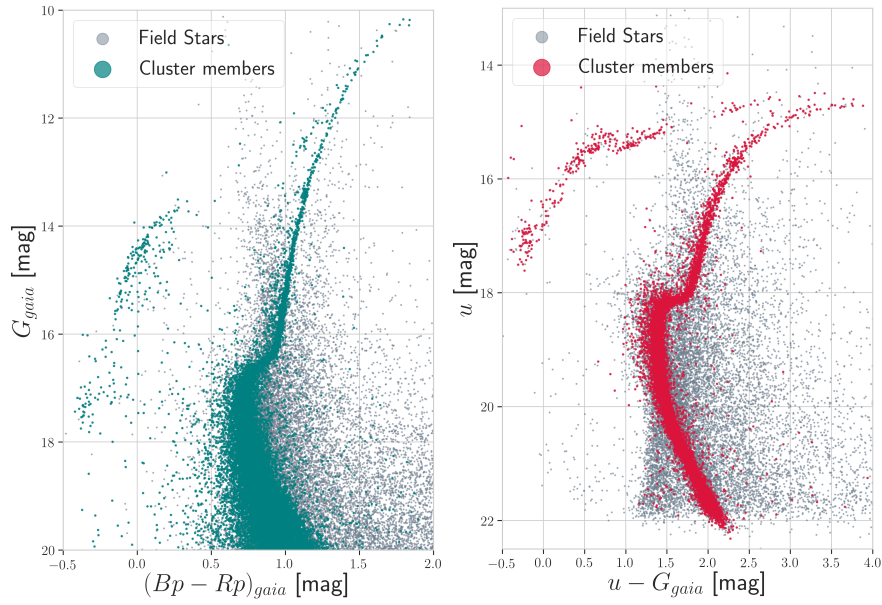


Figure 4.5: CMDs produced using Gaia magnitudes. In the left panel, the extended horizontal branch of the catalog with G- and M-jumps is easily discernible. In the right panel, as the u-filter is used, the EHB is more prominent. How the cluster members were chosen is explained in Section 5.1

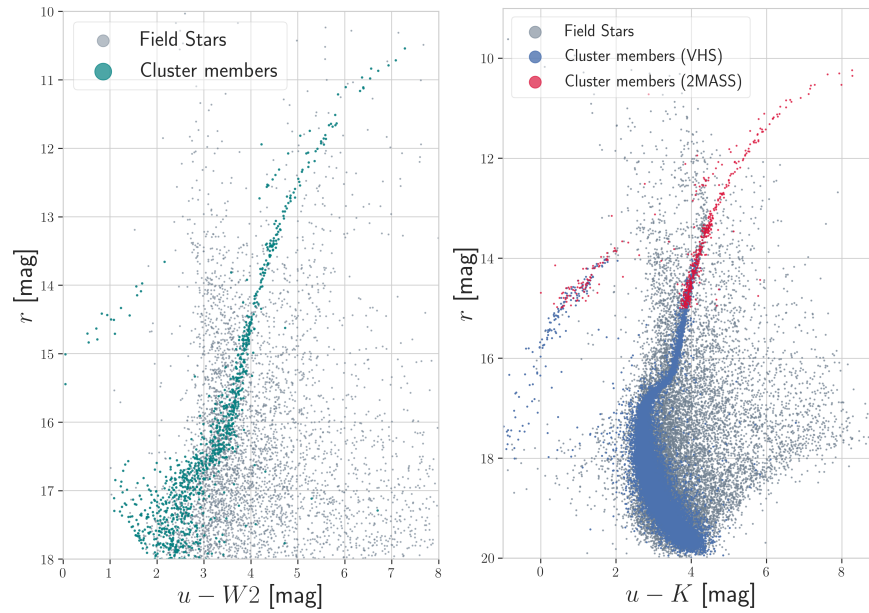


Figure 4.6: (Left) A color magnitude diagram produced using the WISE W2 magnitude. As stars which have considerable emission in the u-filter wavelengths (~ 360 nm) will have a very low magnitude in the mid-IR wavelengths (λ_{eff} for W2 is $\sim 4.6 \mu\text{m}$), the u-W2 CMD is scarcely populated. (Right) A CMD produced using combination of K-filters from 2MASS and VHS. VHS being a contemporary survey, adds a substantial population to the faint end of the CMD. Very bright objects (saturated in VHS photometry) are retained through 2MASS' catalog.

4.4.5 WISE

Wide-field Infrared Survey Explorer (WISE, [Wright et al. 2010](#)) survey was matched to extend our coverage to mid- and far-IR wavelength regions. The separation distance of 0.4 arcseconds was used to match the stars. A CMD produced using WISE W2 magnitude is shown in Figure 4.6.

4.4.6 STETSON’S HOMOGENEOUS PHOTOMETRY

The articulate catalog by Peter Stetson provided in the Homogeneous Photometry series ([Stetson et al., 2019](#)) had a significant overlap with the areal coverage of our survey. Along with the UBVRI magnitudes, the variability index of each star was included in our catalog. Since our photometry had regularly sampled observations, variability indices measured in our photometry were found to be more consistent than the ones given in this catalog.

4.4.7 HUGS

The HST Ultraviolet Globular Cluster Survey ([Piotto et al., 2015](#)) covered only the inner ~ 120 arcminutes of NGC 6752 but the angular resolution of HST allowed us to get magnitudes for those stars which are saturated/blended in our observations. It also allowed us to get a better number density profile of the cluster as explained in Section 5.2.1. The CMDs are shown below.

4.5 CULMINATION

As the cluster is located well below the galactic disk (at a latitude $l = -25.628^\circ$), it suffers from very low reddening ($E(B-V) = 0.046$). However, over the 1×1 degree² field of view of our photometry, it is important to correct for differential reddening (or spatially varying extinction). Therefore, color-excess values for all the stars in our catalog were obtained from the [Schlafly & Finkbeiner \(2011\)](#) extinction maps*. The 2×2 degree² extinction map centred on NGC 6752 is shown in Figure 4.7. These values were incorporated into our final catalog. This master catalog ultimately contained astrometric and photometric measurements for more than 140,000 stars ranging in wavelength from Far-UV to Far-IR. The Spectral coverage of the catalog is presented in Table 4.3.

*<https://irsa.ipac.caltech.edu/applications/DUST/>

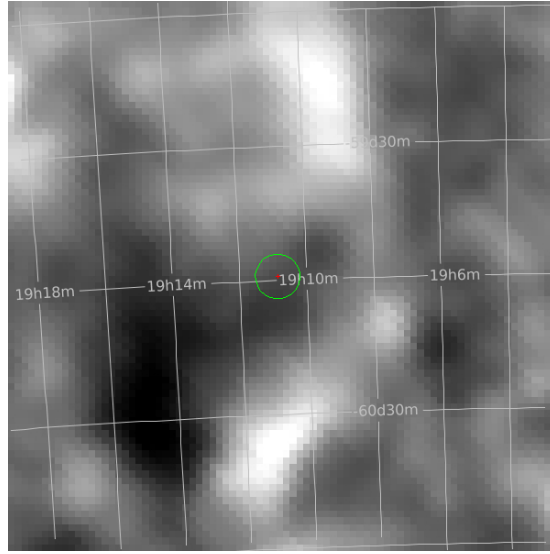


Figure 4.7: A 2×2 degree² extinction map centred on NGC 6752 taken from [Schlafly & Finkbeiner \(2011\)](#).

Table 4.3: List of all the magnitudes in the catalog arranged in ascending order of their filter's effective wavelengths in Å.

Filter	λ_{eff} (Å)	Filter	λ_{eff} (Å)
Galex Fuv	1542	H α	6590
Galex Nuv	2274	i_SDSS	7508
HST 1	2750	Gaia Rp	7588
HST 2	3360	HST 5	8140
u_SDSS	3607	I	8797
U	3656	z_SDSS	8884
HST 3	4350	2MASS J	12350
B	4353	VHS J	12464
g_SDSS	4679	2MASS H	16620
Gaia Bp	5020	VHS Ks	21336
V	5477	2MASS K	21590
Gaia G	5836	WISE W1	33526
HST 4	6060	WISE W2	46028
r_SDSS	6241	WISE W3	115608
R	6349	WISE W4	220883

Initial product:

Single-chip, single-exposure, single-filter catalogs.

End Product:

The final master catalog of all the chips, all the exposures, all the images matched against a whole host of other surveys containing a gamut of information on the various properties of the cluster.

The universe seems neither benign nor hostile, merely indifferent.

Carl Sagan

5

Analysis and Results

A comprehensive photometric catalog of a cluster presents a treasure trove of information waiting to be unravelled. This chapter explains how the member stars of the cluster were selected from our catalog. These members were used to obtain the number density profile of the cluster and perform its dynamical modelling and derive other pertinent parameters.

5.1 MEMBERSHIP

A double-edged mechanism was used to select the member stars from all the stars observed in the 1×1 degree² field of view. Initially, a fiducial sequence was computed in the i vs $r-i$ CMD. All the stars lying within a certain sigmas from the fiducial sequence were selected as preliminary members. Subsequently, these stars were further filtered based on their Gaia proper motions. The cleaning along the CMD was carried out under the knowledge that all the stars in a globular cluster will exhibit similar photometric properties. Additionally, the cleaning in the proper motion plane ensured that the stars moving with cluster are selected efficiently.

5.1.1 CMD CLEANING

The cleaning along the CMD has been widely used to identify and filter out background galaxies (Grillmair et al., 1996). The technique is able to reduce the number of background objects by an order of magnitude in comparison with the total population. As NGC 6752

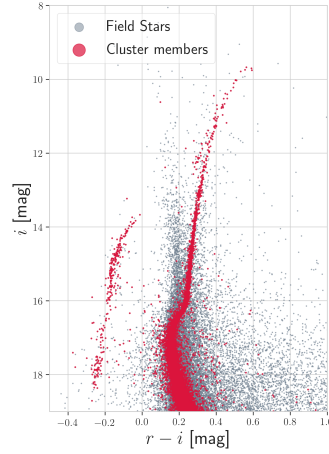


Figure 5.1: A i vs $r-i$ CMD produced using the catalog. As the difference between r and i filters' effective wavelengths is small, the cluster presents a very narrow CMD (as seen by the extent of the X-axis in the plot). The stars displayed as members (in red) are those which are within 18 arcminutes from the cluster's centre and have a total proper motion within 1.5 mas/yr of that of the cluster. This is done for representation purpose only. The members are selected carefully based on the criteria described in the text.

presents a very vertical main sequence and RGB in the i vs $r-i$ CMD (as shown in Figure 5.1), this CMD was chosen as the basis for filtering out the field stars. The entire population was divided into 3 sub-populations. The stars from the bottom of the main sequence to the base of RGB were dealt with independently from the stars lying along the RGB and those lying along the HB.

The stars along the main sequence were binned in groups of 0.15 magnitudes. The median and standard deviation in the $r-i$ color were computed for each group. The median color was selected as a point on the fiducial sequence. This sequence was smoothed using Savitzky-Golay filter (Savitzky & Golay, 1964) and then interpolated using a cubic spline. A $2-\sigma$ boundary on either side of the fiducial sequence was computed using the standard deviation for each bin. These boundaries, too, were smoothed in a similar manner. All the stars within these boundaries were selected as the preliminary members (as shown in Figure 5.2).

This process was then repeated for the RGB and HB populations with slightly different strategies. Firstly, the stars were binned in bigger magnitude bins (0.3 mag) as these regions are scantily populated in comparison with the MS region. Secondly, the acceptance region was computed differently for both the branches.

- For the RGB acceptance region, as the foreground and background sources are more populous than the cluster members, each bin showed a significantly different standard deviation. As a result, an acceptance region of decreasing width from the base of RGB

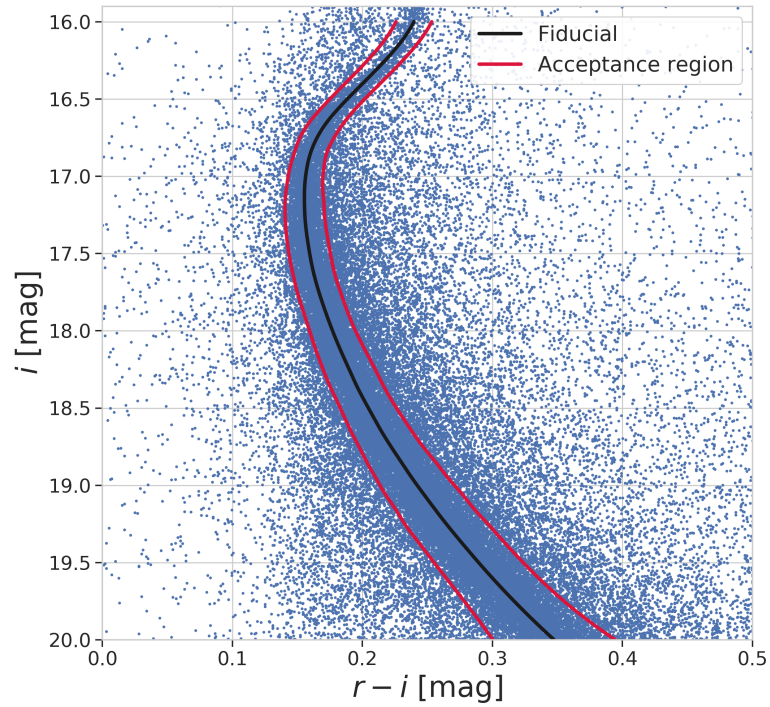


Figure 5.2: The fiducial sequence (in black) traces the population of the cluster very well. The red sequences display the $2\text{-}\sigma$ acceptance region. The stars within this region were selected as preliminary members of the cluster.

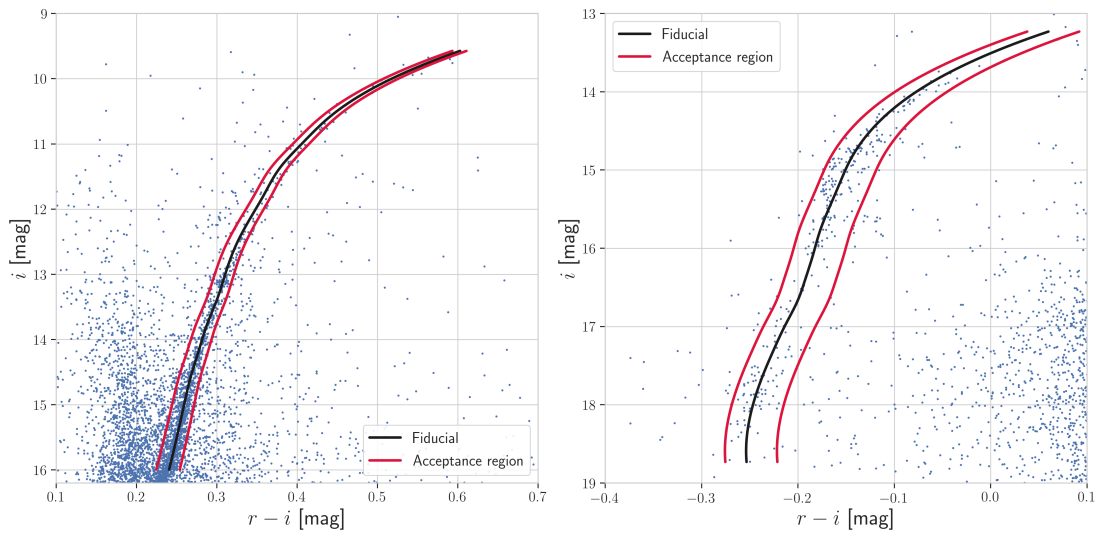


Figure 5.3: (Left) The fiducial sequence (in black) traces the population of the cluster along the RGB. The red sequences display an acceptance region of decreasing width as one ascends the RGB. The stars within this region were selected as preliminary members of the cluster. (Right) The fiducial sequence traces the HB population of the cluster. The red sequences display a fixed-width 0.06 mag acceptance region. In order to account for the G-jump and M-jump discontinuities, a wider acceptance region was established for the HB region.

to the tip of RGB was computed as a function of the i-magnitude (Y-axis).

- As the HBs of GCs display G-jump and M-jump discontinuities (see Section 1.4.3), an acceptance region of a wider width was established. A 0.03 mag width on either side of the fiducial was set up as the acceptance region.

The fiducial sequence and the acceptance region for both the RGB and HB are shown in Figure 5.3. All the stars within the acceptance regions were selected as the preliminary members of the cluster. As the AGB of the cluster is comparatively harder to isolate, the AGB stars of the cluster were picked meticulously by eye (as described in Section 5.5). As there were roughly 30 stars along the AGB with almost all of them located in the internal parts of the cluster, their presence or absence wouldn't have much bearing on the number density profile of the cluster.

Starting from 141,633 stars in the final catalog, the culling process along the CMD resulted in 32,664 being selected as the preliminary members of the cluster. Furthermore, a cut-off of $r = 20$ mag was set up as the faint limit of the catalog to minimize the fraction of spurious detections. This decreased the member population to 29,090. However, it is possible that some of these accepted stars might be the field intruders which just happen to lie along the cluster CMD. In order to remove those, the membership criterion was then refined using Gaia proper motions.

5.1.2 PROPER MOTION CLEANING

With Gaia's proper motion calculations for the stars in our field of view, it was possible to eliminate the background sources detected in the external parts of the cluster. A majority of the preliminarily selected stars had their proper motions measured by Gaia (26,529 out of 29,090). The proper motion in RA (μ_{α^*}) provided by Gaia is already multiplied by the cosine of DEC ($\cos(\delta)$) to factor in spherical geometry. The proper motions ($\mu_{\alpha^*}, \mu_{\delta}$) were plotted against the r-magnitude of the stars and then treated individually.

As seen in Figure 5.5, the median values of μ_{α^*} and μ_{δ} for the cluster were found to be:

$$\mu_{\alpha^*} = -3.187 \pm 0.002 \text{ mas/yr} \quad (5.1)$$

$$\mu_{\delta} = -4.042 \pm 0.002 \text{ mas/yr} \quad (5.2)$$

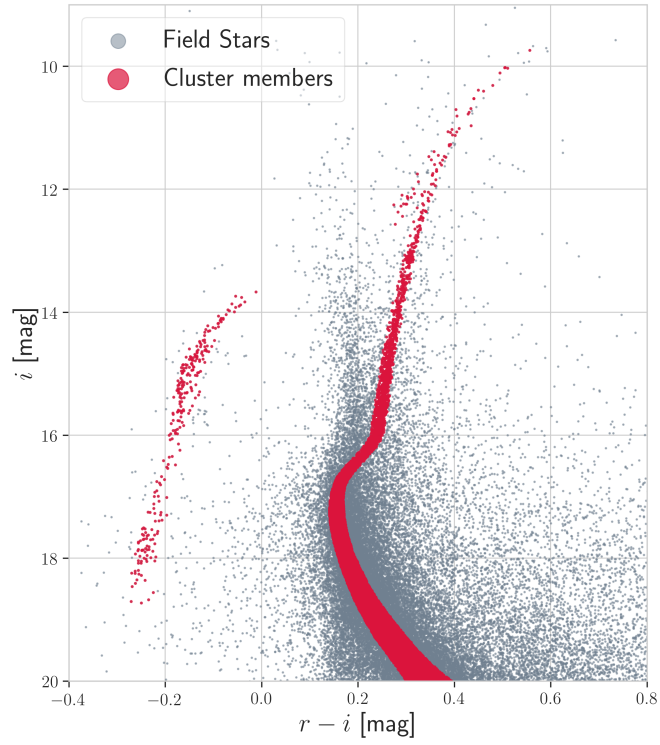


Figure 5.4: Preliminary members of the cluster selected on the basis of acceptance regions established using fiducial sequences.

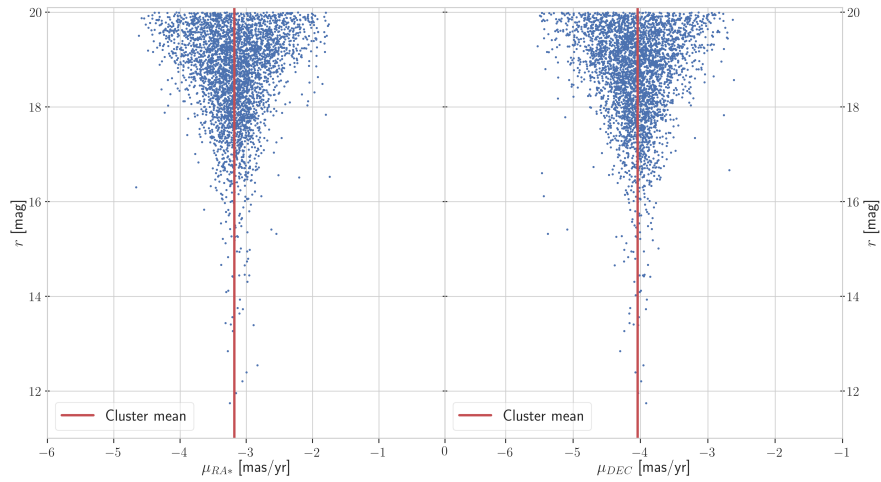


Figure 5.5: The plots of μ_{α^*} and μ_{δ} vs the r-magnitude of the stars. The red lines represent the central values of the cluster. The stars within $3\text{-}\sigma$ of the central values of the binned groups were accepted as members.

Table 5.1: The table displays the number of stars left after every step of the culling process. The numbers in parenthesis are the number of stars without a proper motion measurement.

# of stars in field of view	141633
After CMD cleaning	32664
Brighter than $r=20$ mag	29090
In internal 12 arcmin	23467 (2553)
Farther than 12 arcmin	5623 (8)
External stars after proper motion cleaning	3619
Selected member stars	27286

where the errors represent the uncertainty in the calculation of the median values (standard errors). These calculated values are in good agreement with the values published for NGC 6752 by [Baumgardt et al. \(2019\)](#) (see Table 1.1). These stars were binned in groups of 0.15 mag and the median was found for each group. Any star which had a μ_{α^*} or μ_{δ} greater than the $3\text{-}\sigma$ of the group was rejected (see Figure 5.6).

All the stars within 12 arcminutes from the centre of the cluster were not cleaned using Gaia proper motions, as prescribed by [Vasiliev \(2019\)](#). 2,553 out of the 23,467 stars within 12 arcminutes from the centre did not have a proper motion measurement. Out of the 5,623 stars farther than 12 arcminutes from the centre, only 8 of them did not have a Gaia proper motion measurement; they were provisionally accepted as cluster members. The changes in number of member stars brought about by these cleaning steps have been summarized in Table 5.1. Using this trimmed sample, photometric and dynamic properties of the cluster were inferred as described in the following sections. A plot of RA vs DEC of the selected stars is presented in Figure 5.7.

5.2 NUMBER DENSITY PROFILE

Fitting number density profiles of globular clusters using dynamical models sheds light on their structural properties. In order to compute number density in our cleaned population, it was necessary to deal with (i) the geometry of OmegaCam, as the jitter pattern wasn't enough to cover all the gaps in the CCD array (see Figure 5.7) and (ii) the offset between cluster's centre and the centre of our observation field, as the cluster was centered on Chip 12 of OmegaCAM.

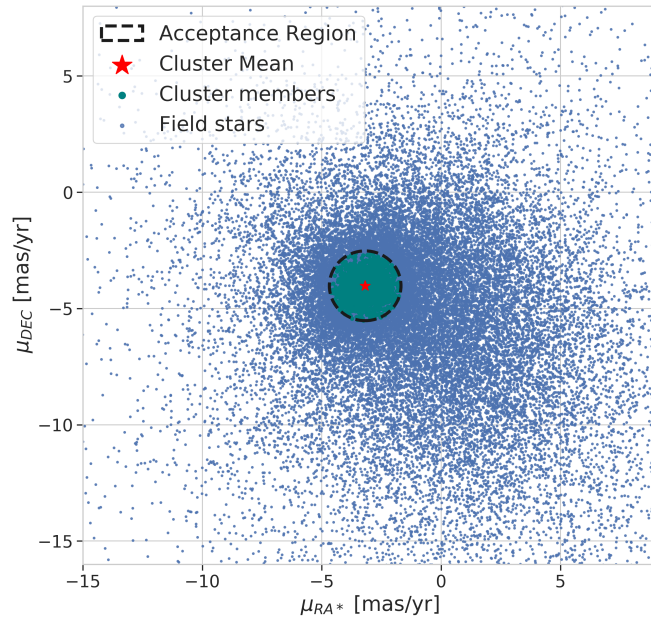


Figure 5.6: Selecting member stars based on proper motions for stars at a distance greater than 12 arcminutes from the centre.

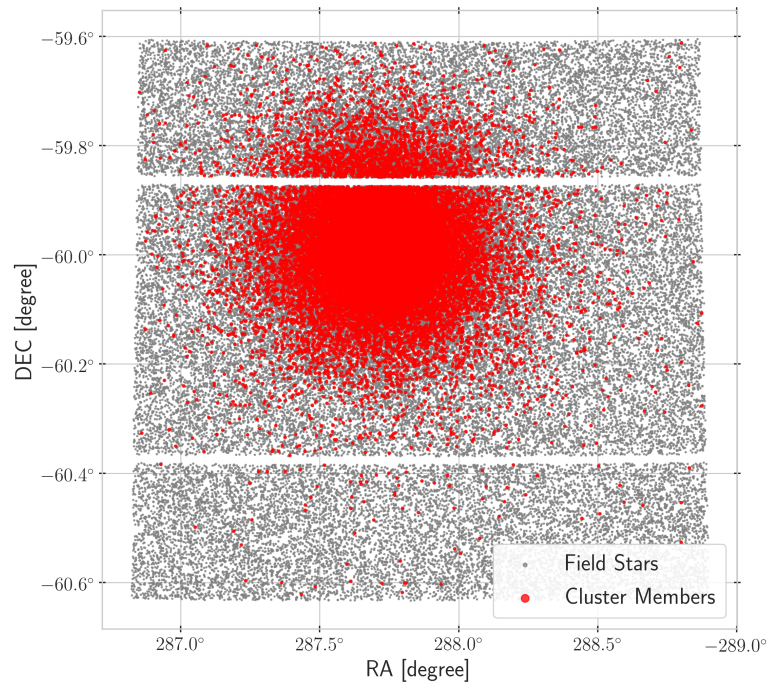


Figure 5.7: The plot of positional coordinates of all the stars selected as cluster members. The 2 horizontal gaps visible close to $\text{DEC} = -59.9^\circ$ and -60.4° emerge due to the geometry of OmegaCAM as discussed in Section 2.2.

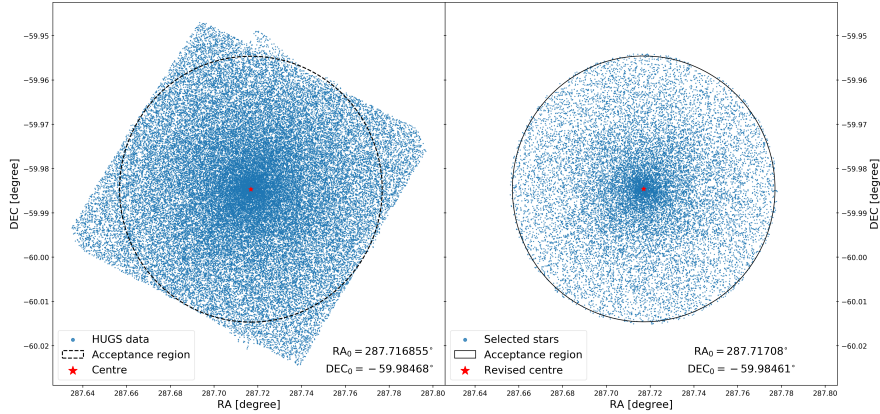


Figure 5.8: (Left) The field of view for HUGS data. A circle of 110 arcseconds centred on the centre of the cluster represents the selection region. (Right) The selected stars with the revised coordinates for the centre shown in red. For details on the calculation of the centre, see text.

To overcome these 2 conditions simultaneously, the projected area used to derive the number density was integrated every time stars were counted. A 2-dimensional grid of points separated by 0.5 arcseconds (roughly 2 times the size of an OmegaCam CCD pixel) was created as a proxy for the field of view of our observations. This was used as the reference plane using which the area was calculated.

Star counts were carried out in 100 radially spaced annuli within 50 arcminutes from the cluster’s centre. Each annulus was propagated to the generated pseudo-OmegaCAM grid and the area was derived by counting the points within the annulus. The final number density plot of our data is shown in Figure 5.10. Due to the extreme crowding and blending of stars in the image, the counts for internal 2.5 arcminutes of the profile are inconsistent. To complement our star counts, we computed the number density profile for the HUGS data.

5.2.1 HST NUMBER DENSITY PROFILE

The Hubble Space Telescope UV Legacy Survey of Galactic Globular Clusters (HUGS, [Piotto et al. 2015](#), [Nardiello et al. 2018](#)), which was matched to our catalog, was used to calculate the number density of the central parts of the cluster. Due to rotation of the telescope, the observational coverage of the cluster was that as shown in Figure 5.8. A circle of 110 arcsecond in radius ensured that maximum number of stars are selected with negligible unobserved area. The blue dots in the right panel of Figure 5.8 represent all the selected stars within 110 arcseconds from the centre.

Due to the high angular resolution of HST data, finding the correct position of cluster’s

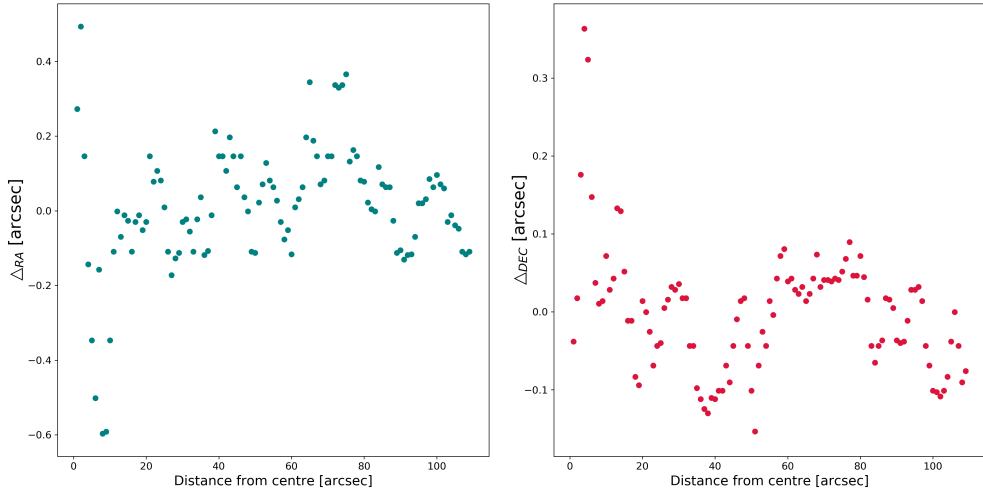


Figure 5.9: The variation in the median position of the centre as a function of the distance from the centre. The offsets Δ_{RA} and Δ_{DEC} have been calculated using the revised centre of the cluster. The scatter is centred around 0.0 arcsec verifying the robustness of the revised position of the centre.

centre was of paramount importance. Any offset between the assumed and the true position of the centre would deviate the derived number density from the actual one. For a preliminary position of the centre, the median of RA and Dec of all the selected stars was computed and assumed as the centre (say RA_0, DEC_0). To refine this position, a simple and effective algorithm was used. All the stars within 1 arcsec from the centre were selected and their median RA and DEC was found. This was repeated for 100 increasing radii between 1 and 110 arcseconds. After every iteration, the RA and DEC was recorded and the offset with respect to RA_0 and DEC_0 was computed. The median of these offsets was added to RA_0 and DEC_0 to get the revised position of the centre of the cluster. The deviation in these offsets with respect to the radius of the selection region is shown in Figure 5.9. The final accepted centre was:

$$\begin{aligned} RA &= 287.717081^\circ \\ DEC &= -59.984612^\circ \end{aligned} \tag{5.3}$$

The number density for HUGS data was calculated in the same way as done for our data. The annuli positioned on the newly-calculated centre were linearly spaced between 0 and 10 arcseconds and logarithmically spaced between 10 and 110 arcseconds. The derived number

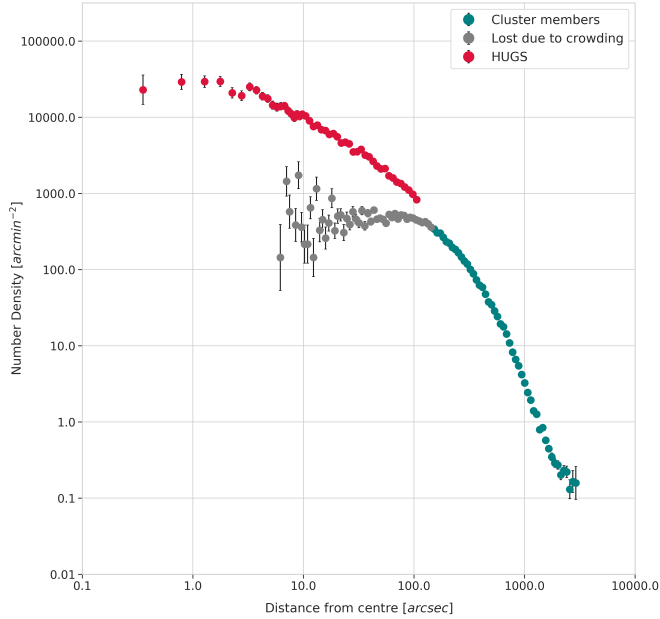


Figure 5.10: Number density profile of the HUGS data for the internal 110 arcseconds of the cluster along with the profile calculated for our data-set. The grey dots represent the cluster members in the internal 150 arcseconds of the cluster lost due to crowding.

density profile is shown in Figure 5.10. The combined number density profile of our data and VST had a gap of 40 arcseconds (from 110 to 150 arcseconds). However, this paltry gap didn't influence the fitting of the dynamic profile.

5.2.2 FITTING DYNAMIC MODELS

For estimating various dynamical properties of the cluster, it is necessary to fit dynamic models to the number density profile of the cluster. Conventionally, globular clusters' density profiles have been well described by the King (King 1966, discussed in Section 1.3) and Wilson models (Wilson 1975, these are spatially more extended than the King models). As discussed in Section 1.3, a self-similar dynamic model is defined using dimensionless radial and density variables. Such a family of models can be reproduced by varying the central potential parameter, c . For fitting these models to density profiles they are projected on to the sky plane.

In order to fit these dynamical models to the calculated number density profile, the package *Lowered Isothermal Model Explorer in Python* (LIMEPY, Gieles & Zocchi 2015)* was

*<https://github.com/mgieles/limepy>

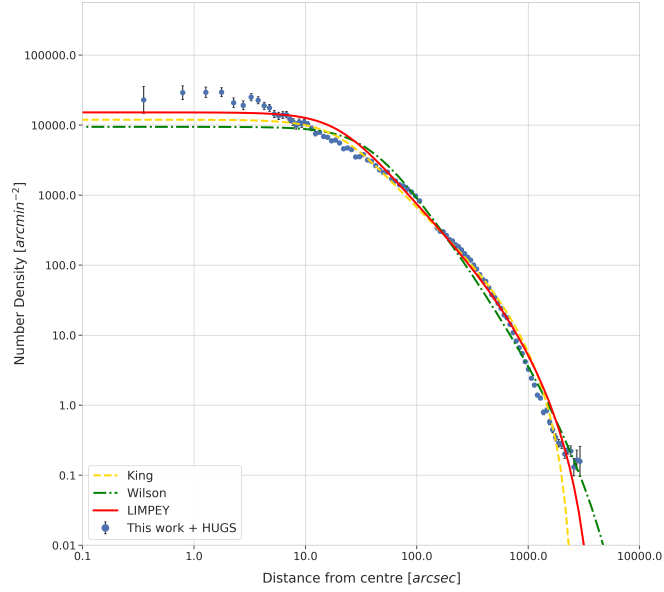


Figure 5.11: The best fitting King, Wilson, and LIMPEY models. The models are described in Section 5.2.2 and the parameters of the fits are given in Table 5.2. The number density profile is the one calculated for HUGS data along with the one computed for our data.

used. The package allowed fitting not only the King and Wilson models, but also custom LIMPEY models. LIMPEY uses 2 parameters to generate different dynamic models:

1. The central potential parameter W_0 which is the proxy for c
2. The truncation parameter g which controls the tidal radius (truncation radii) of the model.

For King models, $g = 1$ and for Wilson models, $g = 2$. The higher the value of W_0 the lower the central concentration is and the higher the value of g , the larger the truncation radius. Except for the central potential, a dynamic model is scaled using the following quantities:

1. Velocity scale σ , which is the one-dimensional velocity dispersion in isothermal models
2. Normalization constant A which controls the density scale of the cluster in 6-d phase space

Table 5.2: Parameters of best fitting King, Wilson, and LIMEPY models. r_c , $r_{h,m}$, and r_t are the model estimated core radius, half-mass radius, and tidal radii, respectively, given in pc.

Model	W_0	g	r_c	$r_{h,m}$	r_t
King	8.80	1	0.28	3.81	33.62
Wilson	7.10	2	0.41	2.05	117.34
LIMEPY	8.36	1.48	0.28	3.01	53.02

The best fitting King and Wilson models were found by computing the reduced χ^2 of their fit to the observed number density profile while using the W_0 , σ , and A as free parameters. For both of these models, the value for g is always constant. However, LIMEPY can generate various lowered models till $g \sim 3.5$. For finding the best-fit LIMEPY model, we included g as an additional free parameter and computed the reduced χ^2 of the fit. The best fitting King, Wilson, and LIMEPY models are shown in Figure 5.11. Table 5.2 shows the parameters of the best fitted models. These parameters are in good agreement with those derived by [de Boer et al. \(2019\)](#) for NGC 6752. The core radius (r_c), half-mass radius ($r_{h,m}$), and the tidal radius (r_t) of the cluster are presented in Table 5.2 and are comparable to those given by [Baumgardt et al. \(2019\)](#) and [de Boer et al. \(2019\)](#). Small values of r_c and $r_{h,m}$ signify that the cluster has a large central potential (a greater central density). As can be seen in Figure 5.11, the King model under-fits the external part of the number density profile while the Wilson model overestimates it. Therefore, the LIMEPY model which had the lowest χ^2 value of the three models, fits the cluster the best.

5.3 ISOCHRONE FITTING

Fitting of the i vs r - i CMD was done using the PAdova And TRieste Stellar Evolution Code models ([Bressan et al. 2012](#), [Chen et al. 2014](#), [Tang et al. 2014](#), [Marigo et al. 2017](#), [Pastorelli et al. 2019](#))[†]. For fitting the isochrones, we transformed our magnitudes to the absolute scale using the following equations:

$$m_0 \equiv m - 5 \log_{10}(d) - \frac{A_\lambda}{A_V} A_V \quad (5.4)$$

$$A_V \equiv R_V \times E(B - V) \quad (5.5)$$

[†]<http://stev.oapd.inaf.it/cgi-bin/cmd>

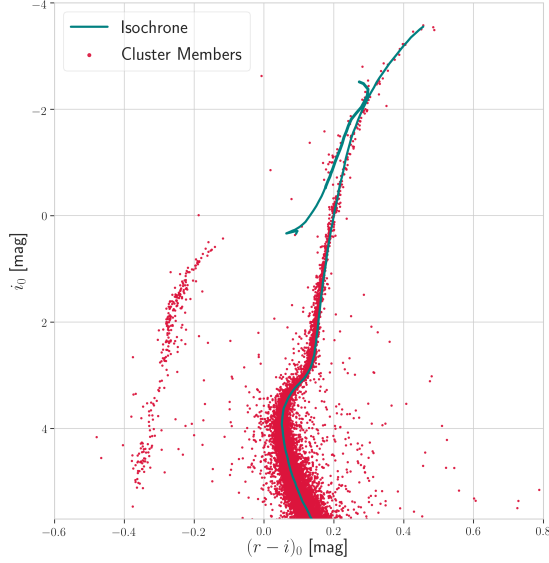


Figure 5.12: The best-fitting PARSEC isochrone in the r , $(r-i)$ CMD.

where m_0 is the absolute magnitude of the star and m is the apparent magnitude. The value for distance d was taken from [Baumgardt et al. \(2019\)](#) as 4.25 pc. The values for absolute extinction A_λ/A_V for OmegaCAM filters were provided in the isochrones. The values for total extinction A_V were calculated on a star-by-star basis using the extinction values obtained for each star (as explained in Section 4.5) and the galactic extinction law value of $R_V = 3.1$ ([Cardelli et al., 1989](#)). The apparent magnitudes were calibrated in the AB magnitude system and OmegaCAM’s photometric system. A plot with the absolute magnitudes is shown in Figure 5.12.

The best fitting isochrone had the following values: $[Fe/H] = -1.46$, Age = 12.6 Gyr, Reimers RGB Mass loss parameter $\eta_{Reimers} = 0.2$, and $Z_\odot = 0.0152$. The best-fit isochrone is shown in Figure 5.12. The parameters of our best-fit isochrone are in good agreement with the values calculated by [Gratton et al. \(2005\)](#) for metallicity and [Gratton et al. \(2003\)](#) for age of NGC 6752.

5.4 H α CMD

The final catalog presents the first extensive H α coverage of NGC 6752. Among the many CMDs producible by our photometric catalog, the H α CMD is particularly interesting. In the r , $(r-H\alpha)$ CMD, we can immediately see signs of H α excess in quite a few stars. The

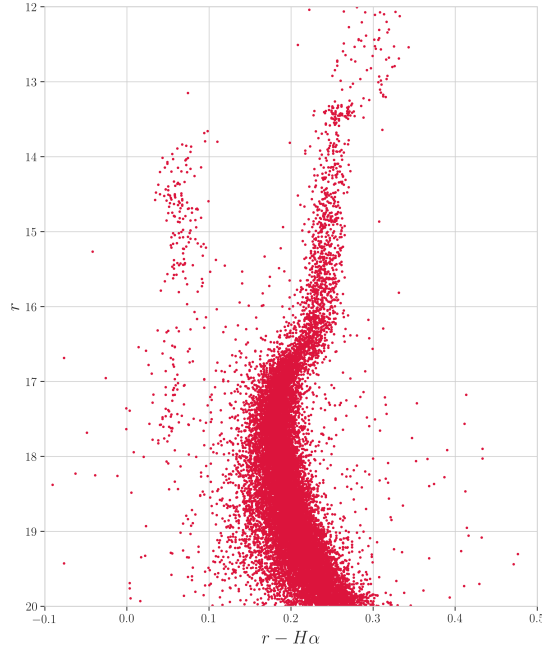


Figure 5.13: The $r, (r-H\alpha)$ CMD reveals potential stars along the main sequence that might be showing excess $H\alpha$ emission.

$H\alpha$ excess is an indicator of magnetic activity and presence of circumstellar disk. Even after cleaning the catalog for the stars present in the vignettted region of the CCD (shown in Figure 2.3), a substantial fraction of the population shows excess emission in $H\alpha$ (see Figure 5.13). However, the time frame of this thesis did not permit any further analysis of these stars.

5.5 STAR COUNTS OF EVOLVED STARS

We counted the number of RGB, AGB, and HGB stars picking them out by eye to avoid any error for our data and the HUGS data. As discussed earlier, the HUGS data covered the internal 110 arcseconds of the cluster. For stars farther away than 110 arcseconds, we carried out star counts using our catalog. The counts of these stars are shown in Table 5.3.

5.5.1 R PARAMETER

Measuring Helium abundance in globular clusters is important for various astrophysical reasons. Different generation stars in a globular cluster show variances in their Helium content. Helium abundance has also been touted as one of the leading candidates for the second parameter of the HB morphology problem (Milone et al., 2018). However, spectroscopically

determining helium abundances in globular clusters is not straightforward as the Helium line can be studied confidently in only few hot stars (for $8,000K \lesssim T_{eff} \lesssim 11,000K$, [Marino et al. 2014](#)).

[Sandquist \(2000\)](#) laid out 3 parameters as indicators of Helium abundance in globular clusters calculable using wide-field deep photometry: the population ratio R ([Iben, 1968](#)), the MS-HB magnitude difference Δ ([Caputo et al., 1983](#)), and the RR Lyrae mass-luminosity exponent A ([Carney, 1980](#)). It has been shown that Δ and A are useful indicators of relative Helium abundance. However, R is an excellent indicator for absolute He abundances. [Cas-sisi et al. \(2003\)](#) were able to constrain the He abundance for galactic globular clusters using the R parameter to a value in good agreement with the primordial Helium abundances.

The population ratio R is defined as:

$$R \equiv \frac{N_{HB}}{N_{RGB}} \quad (5.6)$$

where N_{HB} is the number of horizontal branch stars and N_{RGB} is the number of red giant branch stars brighter than the luminosity level of the HB ([Iben, 1968](#)). This represents the dependence of the hydrogen-burning shell's progress on the hydrogen content of the envelope material being fed into it. To a lesser extent, it reflects the change of helium core mass at helium flash, which affects the HB luminosity, and hence the HB lifetime.

Using the u , ($u-i$) CMD, we were able to identify and select the RGB, HB, and AGB populations of the cluster. They are shown in Figure 5.14. We used literature values of the HB luminosity and chose the RGB stars only above this level. The star counts are shown in Table 5.3. As the distinction between the AGB and RGB can be very tricky, we confirmed their numbers in the g , ($g-K$) CMD (see the right panel of Figure 5.14). The computed value of R is within the errors of the values quoted by [Sandquist \(2000\)](#) for NGC 6752 ($R = 1.56 \pm 0.18$). However, as noted by [Zoccali et al. \(2000\)](#), comparison of values for R computed using different photometries isn't straightforward, owing to uncertainties in bolometric corrections for computing the HB luminosity.

5.5.2 R_2 PARAMETER

The R_2 parameter is defined by [Caputo et al. \(1989\)](#) as:

$$R_2 \equiv \frac{N_{AGB}}{N_{HB}} \quad (5.7)$$

Table 5.3: Star counts and the R and R_2 parameters. Our data-set involved all the stars between 1.8 and 20 arcminutes from the centre of the cluster. The HUGS data was used to compute star counts in the internal 1.8 arcminutes of the cluster.

Data-set	N_{RGB}	N_{AGB}	N_{HB}	R	R_2
Our VST data	129	16	196	1.51	0.08
HUGS	90	17	173	1.92	0.23
Combined	219	33	369	1.68	0.09

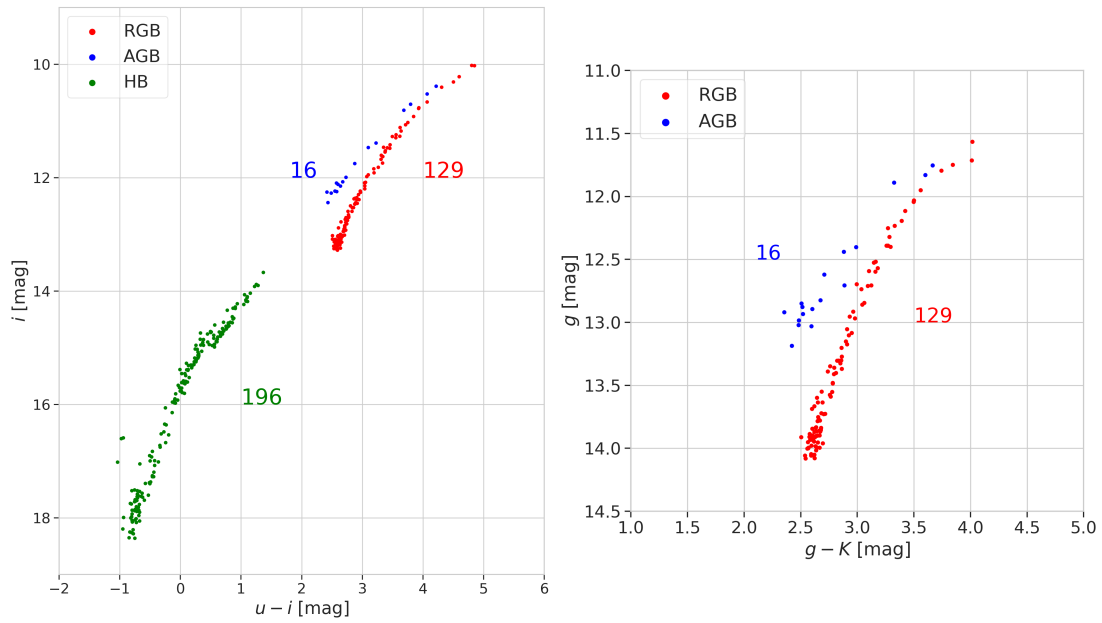


Figure 5.14: (Left) Counting stars along the sequences in the i vs $u-i$ CMD. To confirm the distinction between RGB and AGB populations, they were plotted in the g vs $g-K$ CMD (right panel).

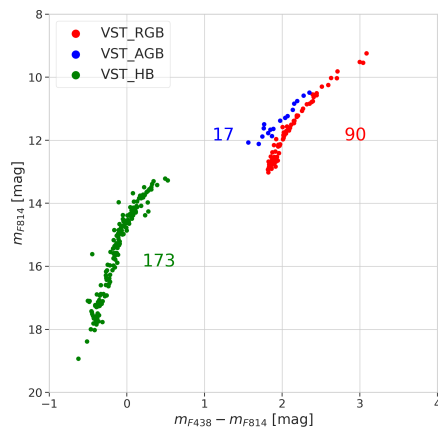


Figure 5.15: Counting stars along the CMD produced using HUGS data.

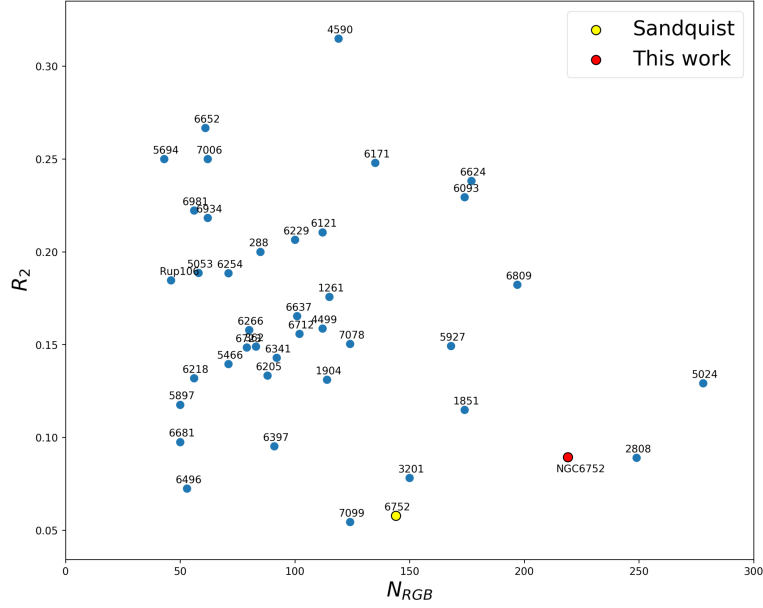


Figure 5.16: The R_2 parameter plotted against N_{RGB} . The R_2 parameter for globular clusters was calculated using the catalog published by Sandquist (2000). All the clusters are members of the New General Catalog (NGC). The prefix has been omitted from the graph for better visualization. The calculated R_2 value for NGC 6752 (shown in red) is almost double that of the original value.

where N_{AGB} is the number of stars in the AGB and N_{HB} is the number of stars in the horizontal branch. This parameter is strongly sensitive to the extension of the convective cores during the HB phase of the stars. Simultaneously, it is fairly insensitive to the initial metal and He abundance of the stars. The theoretical predictions based on the ratio between the AGB and the HB evolutionary timescales made by Cassisi et al. (2003) give a median value of $R_2 \sim 0.12$. Clusters with lowest values of R_2 are those with the bluest HB morphology (Sandquist, 2000) and those with redder HBs exhibit R_2 values closer to the theoretically predicted values.

The R_2 parameter value for NGC 6752 calculated using the combined data-set is 0.09. The surge in this value with respect to that in Sandquist (2000) is shown in 5.16.

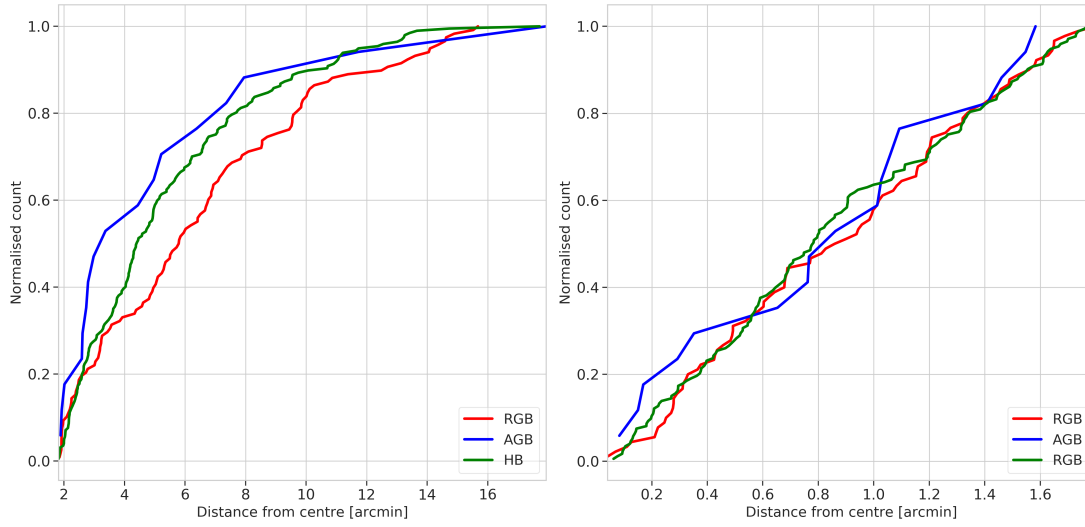


Figure 5.17: (Left) Radial distribution of the evolved stars computed using our data. The normalized cumulative distribution of the stars is shown as a function of the the distance from the centre. The 3 sub-populations deviate slightly locally but overall these deviations are not statistically significant. (Right) Radial distribution of the evolved stars computed using the HUGS data. The 3 sub-populations behave similarly in the internal 1.8-arcminute region.

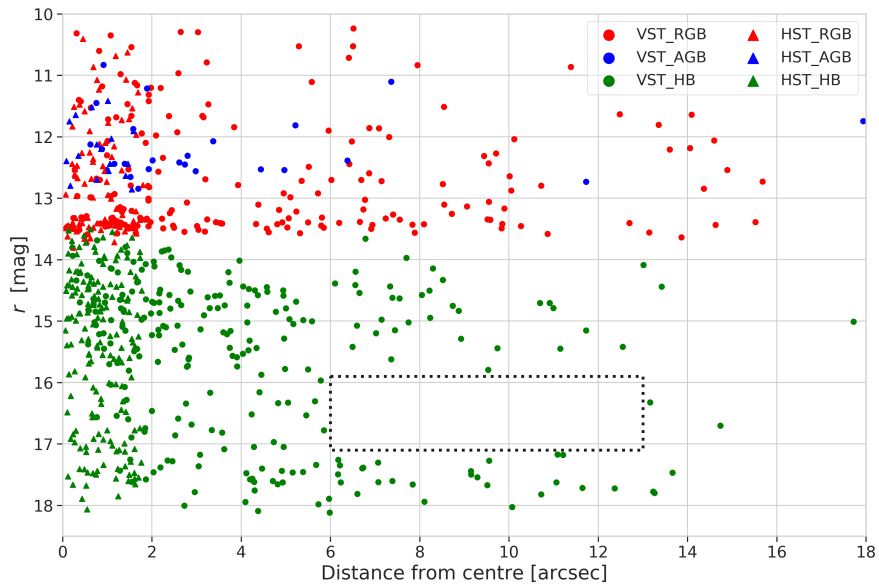


Figure 5.18: The r magnitude of the stars is plotted against their distance from the centre. The HUGS star counts are denoted by triangles whereas star counts for our data are denoted by circles. The black box marks the region devoid of HBs.

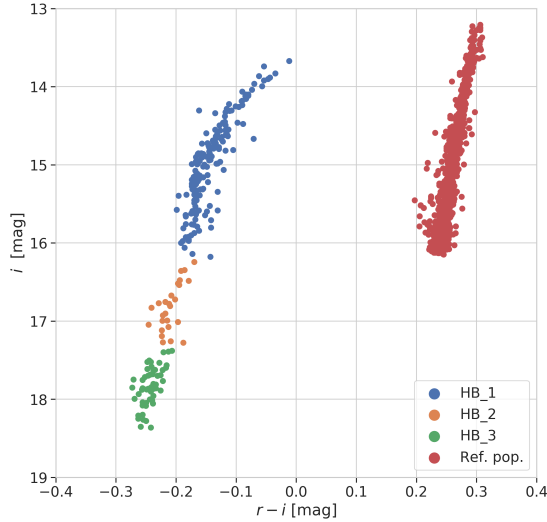


Figure 5.19: The entire HB population was divided into 3 sub-populations based on the magnitude ranges as described in the text. The reference population was chosen along the RGB to normalise the HB counts.

5.5.3 RADIAL DISTRIBUTION

Using the above calculated star counts, stars were sorted by their distance from the centre and their cumulative distribution was computed and normalized. The three distributions shown in Figure 5.17 behave almost similarly. However, when plotting r magnitude of these evolved stars against their distance from the centre - in order to study possible radial trends connected to the distribution of the stars - we noted a possible puzzling observable. As seen in Figure 5.18, a sudden disappearance of HB stars can be seen starting at 6 arcminutes from the center up to at least 13 arcminutes in the magnitude range $16 \lesssim r \lesssim 17$. When compared with theoretical zero-age horizontal branch (ZAHB, [Cassisi & Salaris 1997](#)) models, this magnitude range corresponds to the region comprised between 16,000 K and 22,000 K; i.e., in the region “hotter than the G2-gap at 12,000 K ([Ferraro et al., 1998](#)) and cooler than G3-gap at 20,000 K ([Ferraro et al., 1998](#))”.

Interestingly, stars hotter than the M-jump (or the G3-gap, [Momany et al. 2004](#)) are those which are currently assumed to constitute the Extreme Horizontal Branch (EHB). These stars would not be able to ascend the AGB (AGB-manqué), and therefore the physical mechanism that brought them here (extreme mass-loss and/or He-enhancement) is probably different than the one responsible for the formation of canonical HB stars (stars with $T_{eff} \lesssim 16,000$ K).

Therefore, the region devoid of HB stars between 6 - 13 arcminutes, is also the region de-

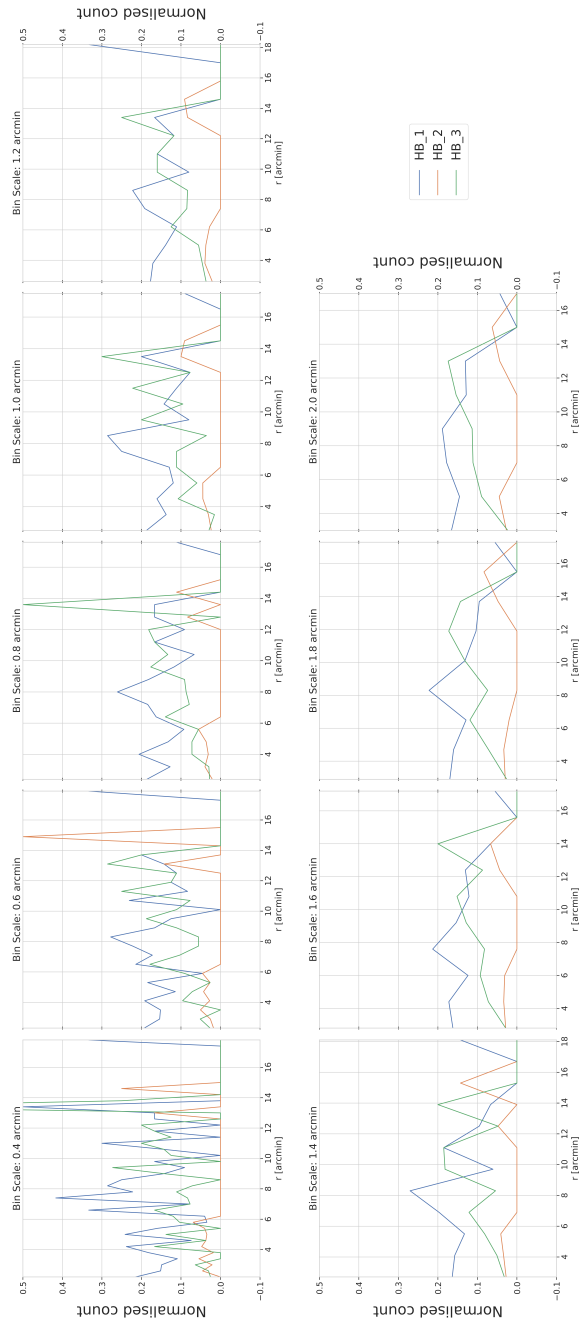


Figure 5.20: The normalised counts of the 3 HB population with respect to the reference RGB population are presented as a function of the distance from the centre (r , in arcminutes). The title of each plot shows the binning scale used to calculate the star counts. The X-axis numbers are the mean values of each of these groups. The various binning scales were used to confirm the statistical significance of the lack of HB stars detected in the region within $\sim 6 - 13$ arcminutes from the centre.

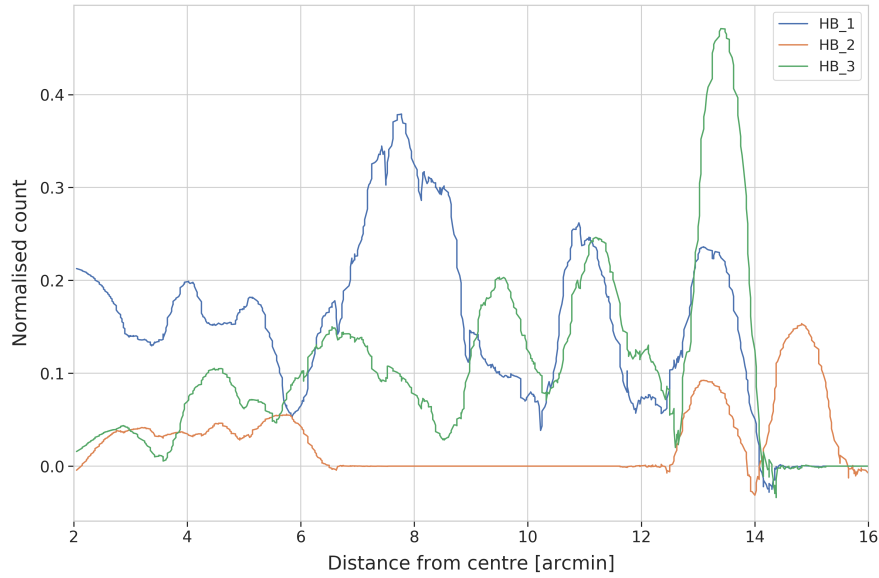


Figure 5.21: The star counts performed for various bin sizes were then combined and smoothed to confirm the statistical significance of the finding. A lack of HB_2 stars is seen in the distance range $\sim 6 - 13$ arcminutes.

limiting the hottest canonical HB stars from the onset of *un-canonical* EHB stars. The reason why this gap is enhanced in the external region (at distances > 6 arcmin) and not within the internal region remains puzzling. However, we could say that it is probably related to the specific dynamical evolution of NGC 6752, as the cluster is known to have gone through an era of core collapse (Djorgovski, 1993).

In order to confirm the statistical significance of this detected paucity of stars, we divided the HB into 3 populations. The first population (HB_1) is chosen as all the stars above 16,000 K. The second population (HB_2, one with the apparent scarcity) is chosen as the one with temperatures between 16,000 K and $\sim 22,000$ K. The third population (HB_3) comprised of all the stars hotter than 22,000 K. The 3 sub-populations are shown in Figure 5.19. Star counts were carried out for these sub-populations with respect to a reference RGB population chosen in the range between the sub-giant branch and the RGB bump. In order to remove the bias of bin size from the star counts, various bin sizes from 0.2 to 2 arcminutes were used. A few of these counts are shown in Figure 5.20. These various counts were combined and smoothed to plot the final radial distribution of these 3 sub-populations. Figure 5.21 confirms that the lack of HB_2 stars is not a mere statistical fluctuation but a significant scarcity.

The universe is under no obligation to make sense to you.

Neil deGrasse Tyson

6

Conclusions

In conclusion, a comprehensive data-set was reduced and an even more comprehensive photometric catalog was extracted out of it. Reduction of the data was carried out using `Alambic`. `SEXTRACTOR` was used to perform preliminary aperture photometry and a routine was developed to calculate full-width at half-maximum of the stars' PSF. `DAOPHOT` was used to perform aperture photometry and compute the PSF of the images. `ALLSTAR` was used for performing PSF photometry of all images. All the independently produced catalogs were matched and combined to form a master catalog of `ugriz` and $H\alpha$ filters. This catalog was matched with external surveys and the final catalog was used for the analysis of the cluster.

Articulate criteria based on Gaia proper motions and fiducial sequences on `r`, (`r-i`) CMD were derived for selecting the members of NGC 6752. Using these selection criteria, number density profile of the cluster was computed. Our density profile was then amalgamated with the newly obtained number densities of the internal 110 arcseconds of the cluster using HUGS data. `LIMEPY` was employed to fit dynamical models such as (King, Wilson, etc.) to the number density profile. Using these models, dynamical properties of the cluster were inferred to be in good agreement with the literature values.

In the reduction of the data, Illumination maps were produced for the Sloan `ugri` filters at OmegaCAM. These new maps can be used for correcting all types of OmegaCam data. The filters at OmegaCAM are stable and hence, the maps can be reused for illumination correction of future data, too. Similarly, new fringing maps produced for the `i`-filter can be used for de-fringing any observations taken with it.

An extensive catalog of NGC 6752 was generated in $H\alpha$ for the first time. In the CMDs produced using $H\alpha$ numerous stars showed excess $H\alpha$ emission. These stars serve as excellent targets for a future spectroscopic study to delve deeper into their nature.

Using our photometry along with the HUGS data, we performed star counts for the stars along the RGB, HB, and the AGB. We calculated values for the pertinent R and R_2 parameters. The radial distribution of these stars was plotted and it was confirmed that these populations behave almost similarly.

However, the star counts also revealed a mysterious missing region in the plot of the stellar magnitudes against the distance of the stars from the centre. This corresponded to the magnitude range ($16 \lesssim r \lesssim 17$) of the discontinuity observed in the EHB. Very few HB stars were observed in this magnitude range at distances greater than ~ 6 arcminutes. Something very peculiar, like the dynamical evolution history of the cluster, could have played a part in the disappearance of HB stars in that region.

The pipeline developed for reduction of the data and photometric extraction of the catalog can be run automatically for other globular clusters observed using OmegaCAM with minimal human input. The Python code has been optimized in such a manner that a 10 terabyte data-sample can be analyzed within 24 hours on a 48-core machine. As a part of a future larger program, we aim to run the pipeline on other southern hemisphere globular clusters observed using OmegaCAM.

Acknowledgments

I would like to thank Simone Zaggia for his other-worldly tutelage. I am honored to have had you as my supervisor. You exude unparalleled passion for science and it's very contagious. I am deeply inspired by your enthusiasm for astronomy and public outreach. I am proud to have been associated with you and I hope you continue to mentor me as I go about my journey in astronomy. I am elated by the fact that I can consider you one of my best friends.

I would like to thank Yazan Momany for being a constant source of guidance. I aspire to imitate your grit and persistence. A substantial fraction of what I have learned over the course of my thesis, I owe it to you. I expect you to keep imparting your knowledge to me.

I thank Giovanni Carraro for your able supervision and for introducing me to Simone and Yazan. I intend to emulate your light-heartedness and punctuality. Thank you for extending so much warmth towards me and for treating me like your son. I extend my gratitude to my referee Antonino Milone for his invaluable insights and encouraging words.

AstroMundus has been as an unexceptionable experience for me and I will always hold it dear. I thank everyone associated with it for making my Master's a satisfactory journey.

I am humbled by the support shown by my family and friends in India. To my mom and dad, I dedicate this thesis to you. I hope you are proud of me. I miss you everyday.

I thank Aishwarya Girdhar for being my family in Europe. Your presence made a world of difference to AstroMundus. You have been a pillar of support for me throughout the past two years. You are a constant source of encouragement and entertainment. I am eternally grateful for your care and affection. I hope our camaraderie stands the test of time. To Fu Chi Yeh and Varun Chaturmutha, I thank you for your solidarity and companionship. Divyanshu Ranjan and Olena Tkachenko, please never cease to be the free spirits that you are. To all my friends and colleagues in AstroMundus, it has been an absolute pleasure knowing you all.

This work would not have been completed within the time that it did without the JUPYTER project (Pérez & Granger, 2007). This work made use of TOPCAT (Taylor, 2005). The national facility capability for SkyMapper has been funded through ARC LIEF grant LE130100104 from the Australian Research Council, awarded to the University of Sydney, the Australian National University, Swinburne University of Technology, the University of Queensland,

the University of Western Australia, the University of Melbourne, Curtin University of Technology, Monash University and the Australian Astronomical Observatory. SkyMapper is owned and operated by The Australian National University's Research School of Astronomy and Astrophysics. The survey data were processed and provided by the SkyMapper Team at ANU. The SkyMapper node of the All-Sky Virtual Observatory (ASVO) is hosted at the National Computational Infrastructure (NCI). Development and support the SkyMapper node of the ASVO has been funded in part by Astronomy Australia Limited (AAL) and the Australian Government through the Commonwealth's Education Investment Fund (EIF) and National Collaborative Research Infrastructure Strategy (NCRIS), particularly the National eResearch Collaboration Tools and Resources (NeCTAR) and the Australian National Data Service Projects (ANDS). This research made use of Astropy,^{*} a community-developed core Python package for Astronomy (Astropy Collaboration et al., 2013; Price-Whelan et al., 2018). This research has made use of the SVO Filter Profile Service[†] supported from the Spanish MINECO through grant AYA2017-84089. This research has made use of NASA's Astrophysics Data System.

^{*}<http://www.astropy.org>

[†]<http://svo2.cab.inta-csic.es/theory/fps>

References

- Arnaboldi M., Capaccioli M., Mancini D., Rafanelli P., Scaramella R., Sedmak G., Vetto-
tolani G. P., 1998, *The Messenger*, **93**, 30
- Astropy Collaboration et al., 2013, *A&A*, **558**, A33
- Bastian N., Lardo C., 2018, *ARA&A*, **56**, 83
- Baumgardt H., Hilker M., Sollima A., Bellini A., 2019, *MNRAS*, **482**, 5138
- Benacquista M. J., Downing J. M. B., 2013, *Living Reviews in Relativity*, **16**, 4
- Bentley J. L., 1975, *Commun. ACM*, **18**, 509
- Bertin E., Arnouts S., 1996, *A&AS*, **117**, 393
- Binney J., Tremaine S., 2008, *Galactic Dynamics: Second Edition*
- Bressan A., Marigo P., Girardi L., Salasnich B., Dal Cero C., Rubele S., Nanni A., 2012,
MNRAS, **427**, 127
- Campbell S. W., et al., 2013, *Nature*, **498**, 198
- Caputo F., Cayrel R., Cayrel de Strobel G., 1983, *A&A*, **123**, 135
- Caputo F., Castellani V., Chieffi A., Pulone L., Tornambe A. J., 1989, *ApJ*, **340**, 241
- Cardelli J. A., Clayton G. C., Mathis J. S., 1989, *ApJ*, **345**, 245
- Carney B. W., 1980, *ApJS*, **42**, 481
- Cassisi S., Salaris M., 1997, *MNRAS*, **285**, 593
- Cassisi S., Salaris M., Irwin A. W., 2003, *ApJ*, **588**, 862
- Charbonnel C., Chantreau W., Decressin T., Meynet G., Schaerer D., 2013, *Astronomy
and Astrophysics*, **557**, L17

- Chen Y., Girardi L., Bressan A., Marigo P., Barbieri M., Kong X., 2014, *MNRAS*, **444**, 2525
- Cordoni G., Milone A. P., Mastrobuono-Battisti A., Marino A. F., Lagioia E. P., Tailo M., 2019, arXiv e-prints, p. [arXiv:1905.09908](https://arxiv.org/abs/1905.09908)
- Di Criscienzo M., Marconi M., Caputo F., 2004, *The Astrophysical Journal*, **612**, 1092
- Djorgovski S., 1993, in Djorgovski S. G., Meylan G., eds, *Astronomical Society of the Pacific Conference Series Vol. 50, Structure and Dynamics of Globular Clusters*. p. 373
- Djorgovski S. G., 1998, *Sky and Telescope*, **96**, 38
- Djorgovski S., King I. R., 1986, *The Astrophysical Journal*, **305**, L61
- Drew J. E., Gonzalez-Solares E., Greimel R., Irwin M. J., et al. 2014, *Monthly Notices of the Royal Astronomical Society*, **440**, 2036
- Ferraro F. R., Carretta E., Bragaglia A., Renzini A., Ortolani S., 1997, *Monthly Notices of the Royal Astronomical Society*, **286**, 1012
- Ferraro F. R., Paltrinieri B., Fusi Pecci F., Rood R. T., Dorman B., 1998, *ApJ*, **500**, 311
- Freeman K. C., Norris J., 1981, *ARA&A*, **19**, 319
- Gaia Collaboration et al., 2018, *A&A*, **616**, A1
- Gieles M., Zocchi A., 2015, *MNRAS*, **454**, 576
- Gratton R. G., Bragaglia A., Carretta E., Clementini G., Desidera S., Grundahl F., Lucatello S., 2003, *Astronomy and Astrophysics*, **408**, 529
- Gratton R., Sneden C., Carretta E., 2004, *ARA&A*, **42**, 385
- Gratton R. G., Bragaglia A., Carretta E., de Angeli F., Lucatello S., Momany Y., Piotto G., Recio Blanco A., 2005, *A&A*, **440**, 901
- Gratton R. G., Carretta E., Bragaglia A., Lucatello S., D’Orazi V., 2010, *A&A*, **517**, A81
- Gratton R. G., Carretta E., Bragaglia A., 2012, *A&A Rev.*, **20**, 50
- Grillmair C. J., et al., 1996, *The Astronomical Journal*, **112**, 1975

Grundahl F., Catelan M., Landsman W. B., Stetson P. B., Andersen M. I., 1999, *The Astrophysical Journal*, 524, 242

Grundahl F., Briley M., Nissen P. E., Feltzing S., 2002, *Astronomy and Astrophysics*, 385, L14

Gullieuszik M., et al., 2015, *A&A*, 581, A41

Harris W. E., 1996, *AJ*, 112, 1487

Herschel W., 1789, *Philosophical Transactions of the Royal Society of London*, 79, 212

Herschel J. F. W., 1864, *Philosophical Transactions of the Royal Society of London Series I*, 154, 1

Iben I., 1968, *Nature*, 220, 143

Kaluzny J., Thompson I. B., 2009, *Acta Astronomica*, 59, 273

King I., 1962, *AJ*, 67, 471

King I. R., 1966, *AJ*, 71, 64

Kraft R. P., 1979, *ARA&A*, 17, 309

Kruijssen J. M. D., 2014, *Classical and Quantum Gravity*, 31, 244006

Kuijken K., 2011, *The Messenger*, 146, 8

Kuijken K., et al., 2002, *The Messenger*, 110, 15

Mapelli M., Sigurdsson S., Ferraro F. R., Colpi M., Possenti A., Lanzoni B., 2006, *Monthly Notices of the Royal Astronomical Society*, 373, 361

Marigo P., et al., 2017, *ApJ*, 835, 77

Marino A. F., et al., 2014, *MNRAS*, 437, 1609

Martin D. C., et al., 2005, *ApJ*, 619

McLaughlin D. E., Harris W. E., Hanes D. A., 1994, *ApJ*, 422, 486

- McMahon R. G., Banerji M., Gonzalez E., Koposov S. E., Bejar V. J., Lodieu N., Rebolo R., VHS Collaboration 2013, *The Messenger*, **154**, 35
- Milone A. P., et al., 2013, *ApJ*, **767**, 120
- Milone A. P., et al., 2018, *MNRAS*, **481**, 5098
- Milone A. P., et al., 2019, *Monthly Notices of the Royal Astronomical Society*, **484**, 4046
- Momany Y., Piotto G., Recio-Blanco A., Bedin L. R., Cassisi S., Bono G., 2002, *The Astrophysical Journal*, **576**, L65
- Momany Y., Bedin L. R., Cassisi S., Piotto G., Ortolani S., Recio-Blanco A., De Angeli F., Castelli F., 2004, *Astronomy and Astrophysics*, **420**, 605
- Mucciarelli A., Lapenna E., Lardo C., Bonifacio P., Ferraro F. R., Lanzoni B., 2019, *The Astrophysical Journal*, **870**, 124
- Nardiello D., Milone A. P., Piotto G., Marino A. F., Bellini A., Cassisi S., 2015, *Astronomy and Astrophysics*, **573**, A70
- Nardiello D., et al., 2018, *MNRAS*, **481**, 3382
- Pastorelli G., et al., 2019, *MNRAS*, **485**, 5666
- Pence W. D., White R. L., Seaman R., 2010, *PASP*, **122**, 1065
- Pérez F., Granger B. E., 2007, *Computing in Science and Engineering*, **9**, 21
- Piotto G., et al., 2015, *AJ*, **149**, 91
- Pooley D., et al., 2002, *The Astrophysical Journal*, **569**, 405
- Price-Whelan A. M., et al., 2018, *AJ*, **156**, 123
- Rejkuba M., 2012, *Astrophysics and Space Science*, **341**, 195
- Renzini A., Buzzoni A., 1986, in Chiosi C., Renzini A., eds, *Astrophysics and Space Science Library Vol. 122, Spectral Evolution of Galaxies*. pp 195–231, doi:10.1007/978-94-009-4598-2_19
- Renzini A., Fusi Pecci F., 1988, *ARA&A*, **26**, 199

- Rubenstein E. P., Baily C. D., 1997, *The Astrophysical Journal*, 474, 701
- Sabbi E., Ferraro F. R., Sills A., Rood R. T., 2004, *The Astrophysical Journal*, 617, 1296
- Sandage A. R., 1953, *The Astronomical Journal*, 58, 61
- Sandage A., Wallerstein G., 1960, *ApJ*, 131, 598
- Sandquist E. L., 2000, *MNRAS*, 313, 571
- Savitzky A., Golay M. J. E., 1964, *Analytical Chemistry*, 36, 1627
- Schlafly E. F., Finkbeiner D. P., 2011, *ApJ*, 737, 103
- Skrutskie M. F., et al., 2006, *AJ*, 131, 1163
- Stetson P. B., 1987, *PASP*, 99, 191
- Stetson P. B., ed. 1993, *Stellar photometry - Current techniques and future developments*
- Stetson P. B., Pancino E., Zocchi A., Sanna N., Monelli M., 2019, *Monthly Notices of the Royal Astronomical Society*, 485, 3042
- Tam P. H. T., Kong A. K. H., Hui C. Y., Cheng K. S., Li C., Lu T. N., 2011, *The Astrophysical Journal*, 729, 90
- Tang J., Bressan A., Rosenfield P., Slemer A., Marigo P., Girardi L., Bianchi L., 2014, *MNRAS*, 445, 4287
- Taylor M. B., 2005, in Shopbell P., Britton M., Ebert R., eds, *Astronomical Society of the Pacific Conference Series Vol. 347, Astronomical Data Analysis Software and Systems XIV*. p. 29
- Thomson G. S., et al., 2012, *Monthly Notices of the Royal Astronomical Society*, 423, 2901
- Vandame B., 2002, in Starck J.-L., Murtagh F. D., eds, *Society of Photo-Optical Instrumentation Engineers (SPIE) Conference Series Vol. 4847, SPIE*. pp 123–134, [doi:10.1117/12.460591](https://doi.org/10.1117/12.460591)
- Vandame B., 2004, University of Nice

Vasiliev E., 2019, *MNRAS*, p. 2030

Wilson C. P., 1975, *AJ*, 80, 175

Wolf C., et al., 2018, *PASA*, 35, e010

Wright E. L., et al., 2010, *AJ*, 140, 1868

Zoccali M., Cassisi S., Bono G., Piotto G., Rich R. M., Djorgovski S. G., 2000, *ApJ*, 538, 289

de Boer T. J. L., Gieles M., Balbinot E., Hénault-Brunet V., Sollima A., Watkins L. L., Claydon I., 2019, *MNRAS*, 485, 4906

van den Bergh S., 2008, *Monthly Notices of the Royal Astronomical Society*, 385, L20